TOROIDAL PHASING OF RESONANT MAGNETIC PERTURBATION EFFECT ON EDGE TRANSPORT IN THE DIII-D TOKAMAK

A Thesis
Presented to
The Academic Faculty

by

Theresa M. Wilks

In Partial Fulfillment
of the Requirements for the Degree
Master of Science in Nuclear and Radiological Engineering

Georgia Institute of Technology
May 2013

TOROIDAL PHASING OF RESONANT MAGNETIC PERTURBATION EFFECT ON EDGE TRANSPORT IN THE DIII-D TOKAMAK

Approved by:

Dr. Weston M. Stacey, Advisor
Nuclear and Radiological Engineering
Georgia Institute of Technology

Dr. Glenn E. Sjoden
Nuclear and Radiological Engineering
Georgia Institute of Technology

Dr. Todd E. Evans
Senior Technical Advisor
General Atomics Energy Group

Dr. Bojan Petrovic
Nuclear and Radiological Engineering
Georgia Institute of Technology

Date Approved: 11/27/2012

ACKNOWLEDGEMENTS

The present work was greatly benefited by Dr. Todd Evans, Senior Technical Adviser at General Atomics, whose expertise and advice made it possible to define and undertake this project. The work of the DIII-D research team was the foundation of the data from which this analysis was based, and my many thanks are extended to all of those at General Atomics, specifically Dr. Richard Groebner and Dr. Thomas Osborne, who aided with the use of the database and interpretation of data. I would like to thank Dr. Weston Stacey for being a great advisor through patient guidance and edification by example, as well as the other members of my committee for their valuable time and contribution to the work.

TABLE OF CONTENTS

LIST OF FIGURES

LIST OF TABLES

Page

LIST OF SYMBOLS AND ABBREVIATIONS

ρ	Normalized Radius
f	Particle Distribution Function
j	Ion species
V	Velocity
e	Electric charge
m	Mass
E	Electric Field
B	Magnetic Field
C	Collision term
S	Source term
Γ	Particle flux
n	Density
ν	Momentum transport frequency
φ	Toroidal direction
θ	Poloidal direction
r	Radial direction
p	Pressure
τ	Characteristic time
D	Diffusion coefficient
T	Temperature
$<\sigma v>$	Charge exchange averaged cross section
q	Heat flux
χ	Thermal diffusivity

SUMMARY

Resonant Magnetic Perturbation (RMP) fields produced by external control coils are considered a viable option for the suppression of Edge Localized Modes (ELMs) in present and future tokamaks. Repeated reversals of the toroidal phase of the I-coil magnetic field in RMP shot 147170 on DIII-D has generated uniquely different edge pedestal profiles, implying different edge transport phenomena. The causes, trends, and implications of RMP toroidal phase reversal on edge transport are analyzed by comparing various parameters at $\phi=0°$ and $\phi=60°$ with an I-coil toroidal mode number of n=3. An analysis of diffusive and non-diffusive transport effects of these magnetic perturbations in the plasma edge has been performed. The change in the diffusive and non-diffusive transport in the edge pedestal for this RMP shot is characterized by interpreting the ion and electron heat diffusivities, angular momentum transport frequencies, ion diffusion coefficients, and the pinch velocities for both phases.

CHAPTER 1

BACKGROUND

There is a present drive for development of carbon-free power production as a sustainable solution to the growing energy demand. Magnetic confinement fusion reactors are anticipated to be a viable means to generate base load power for the grid, while eliminating the concerns of long term storage of spent fuel which plagues current fission reactor technology. There is a worldwide collaborative effort for the construction of the International Thermonuclear Experimental Reactor (ITER) [1] presently being built in Cadarache, France. Much of the research in the field of plasma physics uses smaller research tokamaks around the world to validate as well as finalize the design for ITER. One such tokamak in the United States is DIII-D, which is operated by General Atomics in San Diego, California. The present work has used experimental data from DIII-D as a basis for interpretive modeling.

Toroidal Plasmas

A tokamak is a toroid designed to confine plasmas via strong magnetic fields produced by external coils. Figure 1 shows a cross section of the DIII-D tokamak, from which the data was gathered for the present work. The external magnetic field coils can be seen along with the plasma chamber and divertor plate used to capture particles that are no longer confined by the magnetic fields.

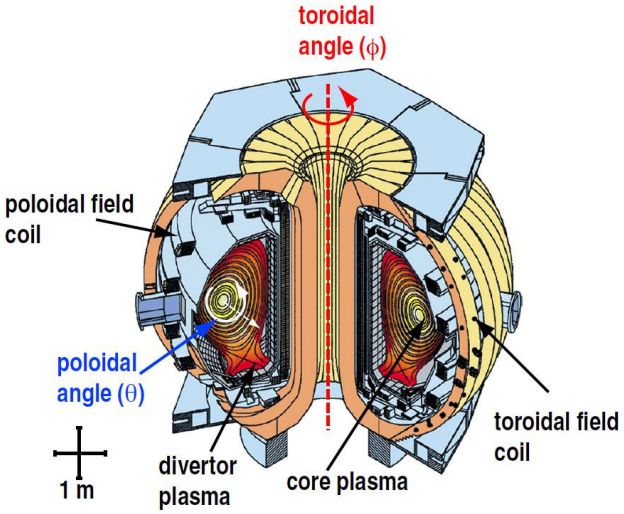

Figure 1: DIII-D tokamak cross section showing toroidal and poloidal magnetic field coils and plasma chamber [2].

Fusion plasmas in tokamaks like DIII-D are exposed to extreme conditions like large densities (~ 10^{20} particles per cubic meter), high temperatures (~10 keV), large currents (a few MA), and strong magnetic fields (a few Tesla). The simplest form of magnetic confinement fusion uses electromagnetic forces to guide deuterium or tritium ions and electrons along magnetic field lines. If the plasma environment has sufficient temperature and density, then fusion will occur. The toroidal plasma is confined by the superposition of two magnetic fields in a device called a tokamak, whose coordinate system is described by orthogonal unit vectors r, θ, and φ, which respectively represent the radial, poloidal, and toroidal directions. The plasma is confined inside the tokamak by magnetic fields in two of the three directions: toroidal and poloidal, as shown in Fig. 2.

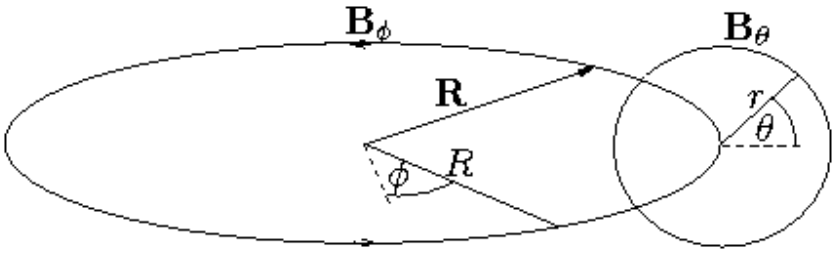

Figure 2: Toroidal and poloidal magnetic fields in a toroidal geometry.

The toroidal magnetic field is externally applied, and the poloidal magnetic field is induced by a toroidal current, yielding a helical shape to the superposition of the magnetic fields lines. There is typically no magnetic field applied or induced in the radial direction, however, the present research will involve investigating plasmas with an oscillating radial magnetic field.

Magnetic Flux Surfaces

Ions and electrons in toroidal geometries are confined in equilibrium to concentric toroidal surfaces on which pressure is uniform. Due to plasma equilibrium described by Maxwell's equations and Ohm's Law, the magnetic field lines are confined to these toroidal surfaces, therefore also confining the particles guided by these field lines. Thus, the surfaces shown in Fig. 3 are known as flux surfaces.

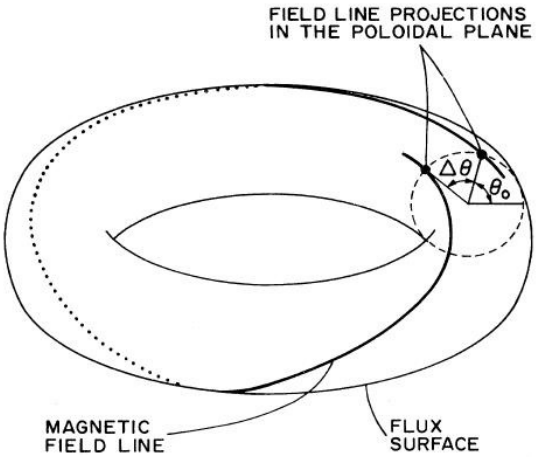

Figure 3: Toroidal flux surface depicted by tracing a magnetic field line once around the torus.

There are two types of flux surfaces that may arise in tokamaks: rational and irrational. Rational flux surfaces occur when the helical magnetic field line is closed, forcing a particle to have the same initial and final point for its trajectory after m toroidal and n poloidal transits around the torus. These trajectories are said to be on rational surfaces described by the safety factor q = m/n. The magnetic perturbations discussed in this work will be of toroidal mode number n = 3, and therefore have resonances on flux surfaces where q = m/3.

The Edge Pedestal

Collisions tend to cause particles to be displaced from one flux surface to another. After many of such collisions, the average trajectory of a particle may have a radial component. Caused by random motion, this process is diffusive by nature and can be described by classical diffusion theory. However, in the outer 10-15% of the plasma, near the vacuum vessel wall, simple diffusion theory does not hold, and instead there is a balance of outward diffusive transport and inward “pinch” transport [3] due to electromagnetic forces.

The plasma edge has piqued the interest of researchers in the past few decades as playing a major role in global performance of the tokmak plasma. Sharp gradients arise in

density, temperature, current, and pressure profiles over a region of a few centimeters just inside the last closed flux surface that cause unique transport phenomena as well as magneto-hydrodynamic instabilities. These steep gradients form an insulation boundary to the plasma core referred to as the transport barrier. The physics that occurs in this edge pedestal region controls the edge gradients, and therefore controls the confinement (such as high (H) or low (L) modes) of the plasma as a whole. Edge pedestal physics, the transition between L and H mode, as well as magneto-hydrodynamic instability suppression is not yet completely understood, and is a present topic of interest in the fusion plasma physics community, especially with regard to the design of ITER.

CHAPTER 2

INTRODUCTION

In the 1980's, a regime of enhanced plasma confinement, called H-mode, was discovered in the ASDEX tokamak in Germany [4]. The ratio of plasma pressure to magnetic pressure, defined as β, is used to characterize the economy of the reactor by comparing fusion power output obtained with energy investment in magnetic fields. H-mode can be obtained in high β plasmas, which increases the plasma core profiles such as temperature, pressure, and density. These profiles are said to sit on a "pedestal" because the core values are relatively constant, then drastically decrease at about 90% of the plasma radius, generating large gradients in the edge region. Along with the increase in plasma core profiles, H-mode plasmas have better energy confinement times by about a factor of two larger than those in L-mode, or Low confinement mode. This enhanced confinement is attributable to the generation of an energy transport barrier, whose formation is not yet fully understood. However, the superior confinement in H-mode comes with a price. Magneto-hydrodynamic instabilities called "edge localized modes" (ELMs) arise in H-mode and are caused by large pressure gradients and currents in the edge pedestal region. The ELM stability boundary is called the peeling-ballooning mode limit because of the trade-offs between destabilization of peeling modes due to current and ballooning modes due to pressure gradients. If this peeling-ballooning threshold is breached, then the ELM occurs, spewing plasma particles and energy from the edge region over a very short time interval [5]. The ELM degrades confinement and introduces detrimentally high heat and particle fluxes to the first wall and the divertor plate. The

edge pedestal profiles then regenerate and enhanced confinement is regained until the peeling-ballooning limit is reached again, triggering another ELM. This is a cyclical process that can occur at varied frequencies and magnitudes. Although harmful to the plasma facing components, the radial transport and impurity control that ELMs can provide is beneficial [6]. Type I ELMs are the most intense variety [5] and are of crucial concern for future fusion devices such as ITER.

Resonant magnetic perturbations (RMPs) have been identified as a means for both mitigating and suppressing ELMs while maintaining a steady state H-mode plasma [7]. External magnetic fields are applied to the tokamak by running current through three dimensionally placed coils outside of the first wall but inside the vacuum vessel. The RMP acts to decrease the density by inducing radial particle transport [8]. Decreasing density acts to lower the pressure, where high pressure and current driven by pressure gradient are a main driver for the ELM instability. ELMs can therefore be mitigated or suppressed while still maintaining particle streaming for impurity control to some extent.

There has been widespread research on the effect of RMP on toroidal plasmas over the past decade. Edge pedestal profiles have been analyzed between similar RMP and H-mode shots [9] by comparing density and temperature profiles, confinement times, and particle discharge on the diverter plate [10], as well as the role of particle pinch in the generation of a transport barrier for both scenarios [8]. Active control methods have been investigated to manipulate the safety factor profile in order to determine the window of resonance operation when ELMs are suppressed [11]. The dependence of the effect of RMP on plasma shape [12] and collisionality [13] has been investigated with particular interest to ITER similar scenarios. In addition, spiraling magnetic field lines can generate

regions of null magnetic fields called islands. The effect of RMP on magnetic islands and overlapping islands to generate an edge stochastic region has also been assessed [14]. There has been previous research on the effect of RMPs on magnetic braking via electromagnetic torque using resonant harmonics in the applied field as well as the neoclassical toroidal viscosity model by applying non-resonant harmonics [15, 16].

Prior analysis of RMP with respect to H-mode, safety factor, plasma shape, collisionality, toroidal rotation, and edge stochastic regions has laid the groundwork for designing the RMP layout for ITER. However, the theoretical foundation of changing the toroidal phase of the current producing the RMP in DIII-D is not fully understood. There are toroidal asymmetries in the magnetic field in DIII-D, which are a probable cause for different transport in the edge and the generation of unique edge pedestal profiles. The purpose of the present work is to examine this difference in edge transport between perturbations that have been applied with different toroidal phases, or resonant magnetic fields generated by currents flowing through external coils in different directions.

The RMPs considered in this paper are of toroidal mode number n=3 that resonate in the edge region to enhance ion transport and decrease electron density and pressure [11], but do not greatly affect the core of the plasma. Future work includes applying the present analysis to a similar RMP shot in DIII-D with a nulled out interference, or n=0, in the RMP fields between toroidal phases to determine if similar trends occur.

In this thesis, basic conservation laws of particle, momentum, and energy balances are employed to interpret both diffusive and non-diffusive transport from measured density, temperature, and rotation velocity profiles in the edge pedestal using previous theory set forth by Stacey[3]. Interpretation of transport parameters such as

diffusion coefficients, pinch velocities, and momentum transfer frequencies is used with the balance theory [3] as a constraint for experimental data to characterize the dominant mechanism for particle transport at each toroidal phase. The motivation for this work is to understand the fundamental transport changes caused by varying the I-coil phase in order that this awareness can be exploited in future reactors to suppress ELMs in the most effective way.

CHAPTER 3

RESONANT MAGNETIC PERTURBATIONS

Resonant magnetic perturbations are produced by magnet coils located outside of the first wall of the tokamak. These externally produced non-axisymmetric radial magnetic fields are manipulated to control edge pedestal plasma profiles, which result in the mitigation or suppression of ELMs. The RMP can be used to lower the magnitude and increase the frequency of ELMs to lessen in the impact on plasma facing components, or in some cases completely stifle the ELMs altogether.

The physical mechanisms relating to how the RMP changes these plasma parameters are only beginning to be understood. The RMPs tend to decrease the edge pedestal density [8], which in turn decreases the pressure to below the peeling-ballooning mode ELM instability threshold. One theory behind this concept is that the RMP produces a "density pump-out" [17] in the edge region, which uses particle streaming radially outward along the perturbed field lines as a mechanism for diminishing density, and therefore ELM suppression. Another possibility is that radial excursion of the magnetic field lines provide a "braking" of the plasma rotation which affects the plasma force balance. There are many ways to apply such a resonant perturbation, and the next step is to determine the most effective way to suppress ELMs while maintaining impurity control, particle streaming, and energy confinement.

Characteristics of DIII-D Shot 147170

Different resonant magnetic perturbations are produced in DIII-D by changing the parity, magnitude, and toroidal phase of the externally applied magnetic fields. The two types of correction coils used are C-coils and I-coils. As shown in Fig. 4, the C-coils are located parallel to the DIII-D tokamak axis outside of the vacuum vessel wall. Six I-coil

pairs, each with one upper loop and one lower loop, are located toroidally symmetrically around the plasma outside of the plasma chamber wall. The RMP is said to have even parity when the current in the upper and lower coils of each pair is flowing in the same direction and odd parity when the currents are opposite in the upper and lower coils of a coil pair. The toroidal phase of the I-coil field is defined in reference to the direction of current running through the upper coil located at the 30° (clockwise from North) measurement location on the tokamak.

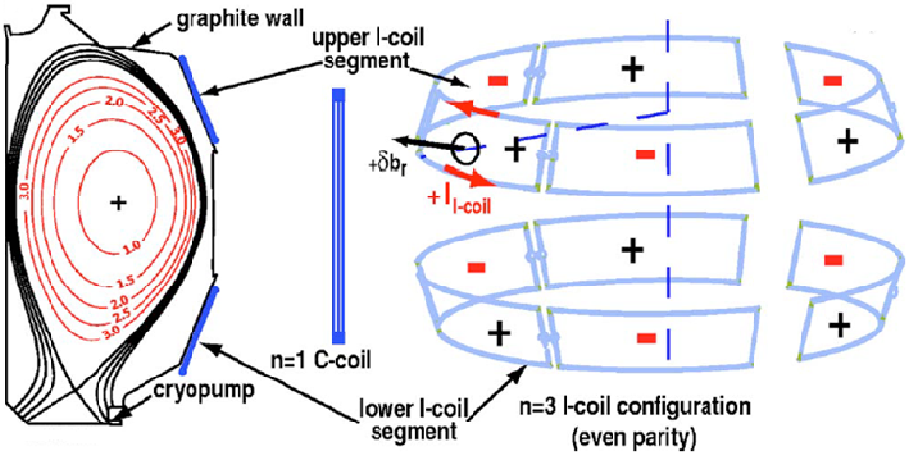

Figure 4: Schematic of I-coil and C-coil magnet locations for DIII-D RMP shot 147170 [19].

DIII-D shot 147170 uses a toroidal mode number n=3 for the I-coils and n=1 for the C-coils for RMP ELM suppression. A mode number of 3 produces a resonance at n=3 rational surfaces such as q = m/n = 11/3. For this shot, the I-coils have even parity and each adjacent set of I-coils produces a radial magnetic field in the opposite direction. Every 200ms, the current in the I-coil reverses direction, and therefore the toroidal phase changes from 0° to 60° or vice versa. This process repeats and generates the resonant magnetic perturbation, along with a change in the edge pedestal transport. Currents running through the I-coil oscillate between roughly –4 kA to +4kA to produce a non-axisymmetric radial perturbation field of about 15G, as shown in Fig. 5. Note that if the

background radial field were axisymmetric, then reversing the toroidal phase between 0° and 60° would only shift the field perturbation by 60°, which would have no effect on the plasma parameters due to the symmetry of the I-coils. However, as indicated in Fig. 5, there is a non-axisymmetric "background" radial field component that constructively interferes with the 0° phase and destructively interferes with the 60° phase angle.

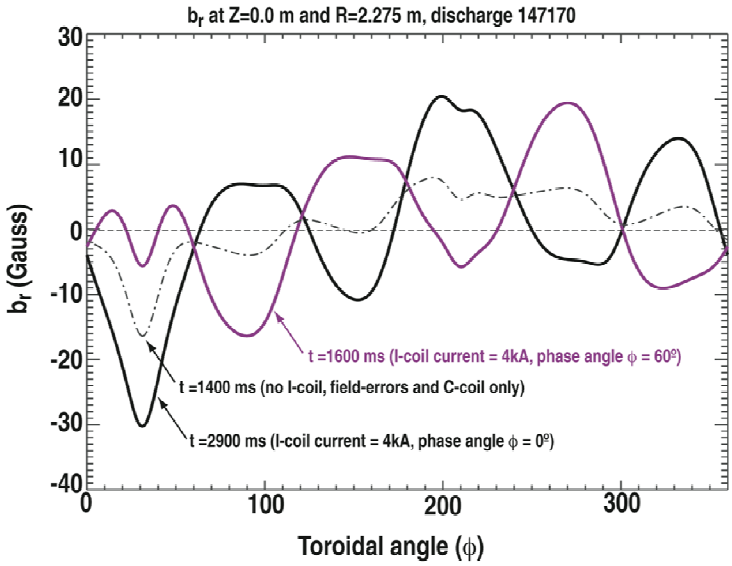

Figure 5: Toroidal dependence of 0° and 60° radial magnetic fields produced by n=3 I-coils. "Background" error field produced by field errors and the n=1 C-coil [20].

The toroidal dependence of the radial perturbed magnetic field is thought to be the cause of the difference between plasma parameters obtained for the 0° and the 60° RMP phases analyzed in this paper. Fig. 6 shows the reversal of the I-coil current in the upper I-coil located at 30 degrees (from North) around the tokamak. Also shown is the measured line average density, whose fluctuations are clearly correlated with the reversal of toroidal phase of the I-coil magnets and likely play an integral role in ELM suppression.

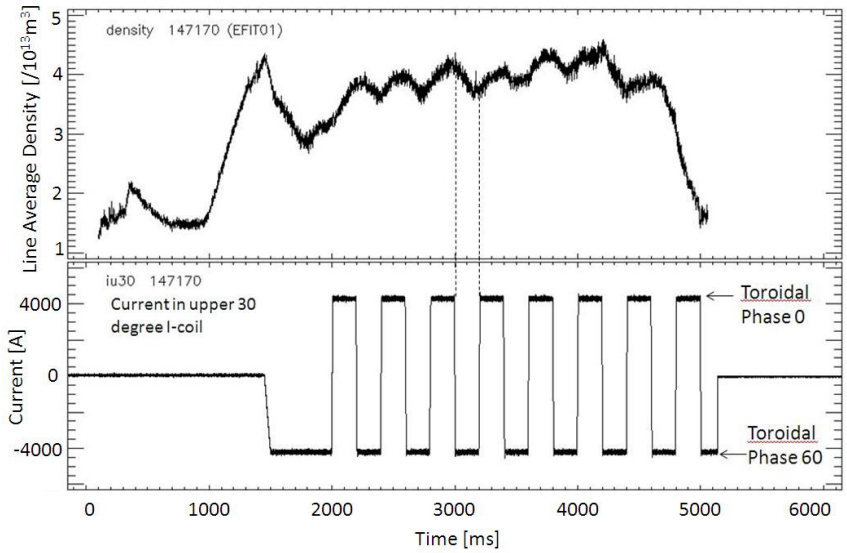

Figure 6: Change in density associated with toroidal phase reversal in the I-coils [20].

Data Analysis

A time slice representing each toroidal phase of the I-coil current was chosen for analysis. The 0° phase is characterized by the time slice 3115-3185ms, and the 60° phase by 3300-3380ms on the time scale shown in Fig. 6. Core plasma parameters remain relatively stable during these time slices [20], making differences in pedestal parameters likely to be most influenced by the toroidal phase of the RMP currents and not by fluctuations in plasma core parameters. Appendix C may be referenced for experimental plasma parameters obtained for each time slice for both toroidal phases.

Data for each time slice was obtained from the DIII-D database [18], and spline fits of the data collected from the Charge Exchange Recombination (CER) system [21] were used to define the carbon ion impurity fraction, temperature, and toroidal and poloidal velocity profiles. Hyperbolic tangent fits were employed to fit the electron density, temperature, and pressure profiles measured by the Thomson scattering system [22]. As an example, the hyperbolic tangent fits of the electron density and the experimental data is shown in Fig. 7 for both phases. Subsequently, the Osborne-

Groebner codes [23] were used to calculate the scale lengths and time derivates for each profile.

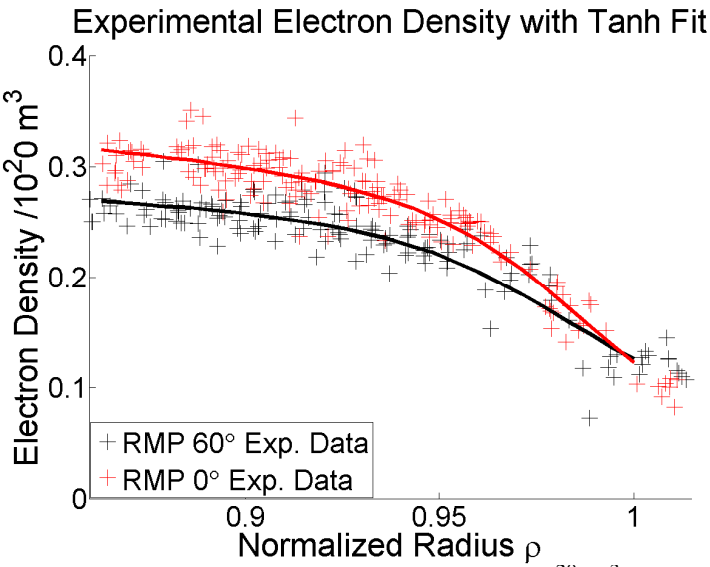

Figure 7: Hyperbolic tangent fit for electron density [10^{20}/m^3] for 0° and 60° I-coil phases.

After relevant parameters were obtained from the DIII-D database and calculated, the GTEDGE pedestal code [24-26] was used to interpret various transport parameters for each time slice. This code performs calculations of three separate boundary conditions for the edge plasma in order to determine the edge pedestal density radial profile. A particle and energy balance on the core to determine the net ion flux across the separatrix. A two-dimensional neutral particle calculation using integral transport theory is used to determine the inward neutral particle flux across the separatrix. After calculating the inward and outward particle fluxes across the separatrix, the ion density at the separatrix is calculated using a "2-point" divertor model calculation. With these boundary conditions defined, the transport of neutrals refueling the plasma edge and the ion density profile are simultaneously calculated [27]. GTEDGE model parameters are adjusted to predict the experimental plasma core line average density, energy confinement time, and central and edge pedestal temperatures.

The elongated and triangular plasma flux surfaces are modeled using an effective circular model that assumes a poloidal average. Eq (1) describes the transformation between the effective radius and the actual radius using the plasma triangularity, κ.

$$\bar{r} = r\sqrt{\frac{(1+\kappa^2)}{2}} \tag{1}$$

Using this expression, the normalized radius ρ = r/a between ρ = 0.86 and ρ = 1 is divided into twenty-five discrete points, which are the locations where the quantities calculated in GTEDGE are defined. With this adjusted core plasma, the edge particle and energy fluxes can be calculated and used to interpret measured densities, temperatures, and rotation velocities, which can hence be interpreted in terms of the radial electric field, the pinch velocity, the particle diffusion coefficient, and the thermal diffusivities in the edge pedestal.

CHAPTER 4

EXPERIMENTAL DATA

Directly Measured Density and Temperature Profiles

The experimental set up at DIII-D allows for direct measurement of several key parameters used in the analysis of particle diffusion. These quantities include electron and carbon ion density, electron and carbon ion temperature, and carbon ion rotation velocities. The density and temperature profiles for electrons are measured using the Thomson Scattering system [22], and velocity, temperature, and pressure gradient profiles of carbon impurities are measured with the Charge Exchange Recombination (CER) spectroscopy system [21]. The electron density for both 0° and 60° is shown in Fig. 8.

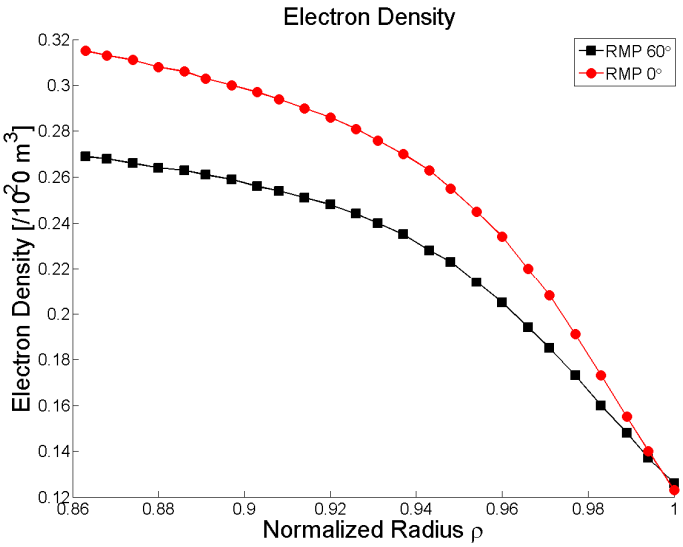

Figure 8: Measured electron density [/ 10^{20} m^3] for 0° and 60° phases.

Higher density and a larger density gradient for the 0° profile generate a more pronounced pedestal located at around ρ = 0.96 as compared to the 60° profile. Because the density profile in the plasma edge is a key contributor to the suppression of ELMs, Fig. 8 will be a reference for comparison to many of the later profiles analyzed.

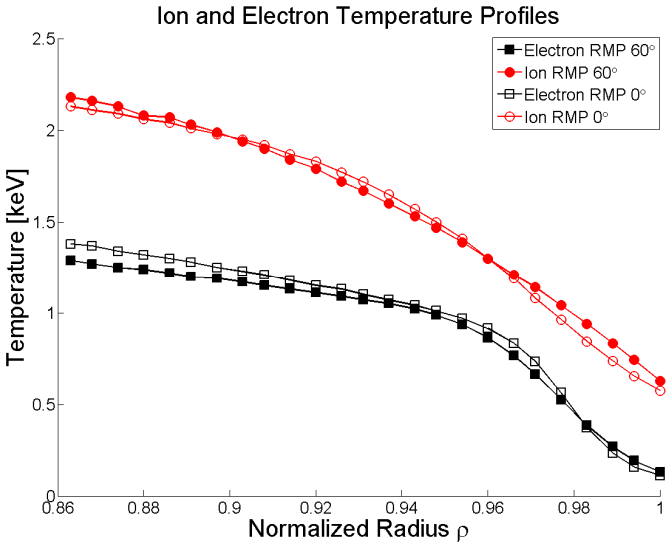

Figure 9: Measured ion and electron temperature profiles as a function of normalized radius.

Ion and electron temperature profiles in Fig. 9 are similar for the 0° and 60° phases. The electron temperature profile has a sharper gradient, giving rise to a pedestal, again around ρ = 0.96. Both phases have suppressed ELMs by RMPs because the product of this temperature profile and the density profile which defines the pressure profile is small enough to be within the peeling-ballooning mode ELM stability limits based on experimental measurement. Stability calculations using the ELITE code are needed to see where these profiles reside with respect to the linear peeling-ballooning stability boundary.

Calculated Parameters: Particle Flux, Radial Electric Field, and Velocity Profiles

Experimental profiles are used with classical conservation law constraints in order to calculate other experimental values as well as infer transport coefficients. Plasma fluid theory based on the first four velocity moments of the Boltzmann transport equation are used as constraints for interpretation of the transport underlying the measured density, temperature and rotation profiles. The constraints on plasma ion transport are 1) particle continuity 2) momentum balance 3) conservation of energy, and 4) heat conductivity. A detailed explanation of these moment equations can be referenced in Appendix A. The generalized Boltzmann transport equation is described by Eq. (2).

$$\frac{\partial f_j}{\partial t} + \boldsymbol{v} \cdot \nabla f_j + \frac{e_j}{m_j}(\boldsymbol{E} + \boldsymbol{v} \times \boldsymbol{B}) \cdot \nabla_v f_j = C_j + S_j \qquad (2)$$

Where f_j is the distribution function for particles of type j. The right hand side of the equation takes into account the loss of particles through collisions, Cj, and particle sources and sinks, Sj. Taking the 0^{th} velocity moment of Eq. (2) and assuming time independence, the first constraint on transport is obtained: particle continuity, or particle flux [3].

$$\nabla \cdot \Gamma = \nabla \cdot n_j v_j = S_j \qquad (3)$$

Where S_j is the source, and includes ionization sources, as well as external particle sources, n_j is the density, and v_j is the velocity. Solving Eq. (3) using the measured data as input leads to the experimental particle flux, given in Fig. 10 for the two RMP phases.

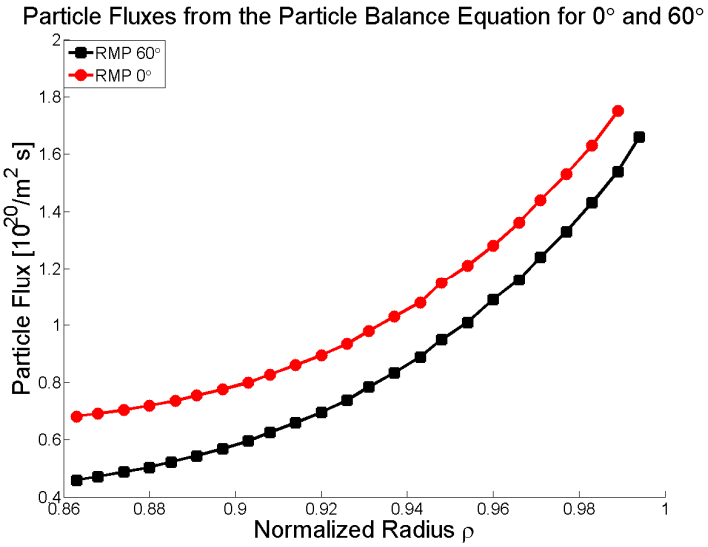

Figure 10: Calculated particle fluxes calculated from the particle balance equation for 0° and 60°.

The particle flux in the radial direction is larger for the 0° phase than for the 60° phase, consistent with the larger particle density for the 0° phase in Fig. 8.

Equation (4) is the generalized 1st velocity moment, which is a constraint on momentum balance [28].

$$m_j \frac{\partial (n \boldsymbol{v}_j)}{\partial t} + \nabla \cdot \boldsymbol{M}_j - n_j e_j \left(\boldsymbol{E} + \boldsymbol{v}_j \times \boldsymbol{B} \right) = \boldsymbol{R}_j^1 + S_j^1 \tag{4}$$

Where $\boldsymbol{M}_j$ is the momentum stress tensor, R^1 is the first velocity moment of the collision term, and $\boldsymbol{S}_j^{\boldsymbol{1}}$ is the first velocity moment of the source term. Assuming time independence and averaging over the flux surfaces, this generalized momentum balance can be decomposed into the toroidal and radial directions, as shown in Eqs (5) and (6), respectively. Equations (5) and (6) are written for a two species model with main ion deuterium species, D, and a carbon impurity, C [29].

$$n_D m_D \left[(\nu_{DC} + \nu_{dD}) V_{\phi D} - \nu_{DC} V_{\phi C} \right] = n_D e_D E_\phi^A + n_D e_D B_\theta V_{rD} + M_{\phi D} \tag{5}$$

$$B_\theta V_{\phi D} = E_r + V_{\theta D} B_\phi - \frac{1}{n_D e_D} \frac{\partial p_D}{\partial r} \tag{6}$$

Where the ν_{dD} are composite momentum transport frequencies that take into account viscosity, inertia, atomic physics, and other "anomalous" processes [29]. $M_{\phi D}$ is an external toroidal momentum source, such as Neutral Beam Injection (NBI), E^A is the induced electric field in the toroidal direction, and all other symbols have their usual meaning.

Carbon rotation velocity profiles are measured with the CER system in DIII-D [21], therefore the radial electric field is the only unknown in Eq. (6) when applying the momentum conservation constraint to the carbon ion instead of the deuterium ion as shown. The expression for the experimental radial electric field is obtained by rearranging Eq. (6) into the form of Eq.(7) [3].

$$E_r = \frac{1}{n_C e_C}\frac{\partial p_C}{\partial r} + V_{\phi C}B_\theta - V_{\theta C}B_\phi \tag{7}$$

The radial electric field is significantly different between the two phases of the I-coil, as shown in Fig. 11.

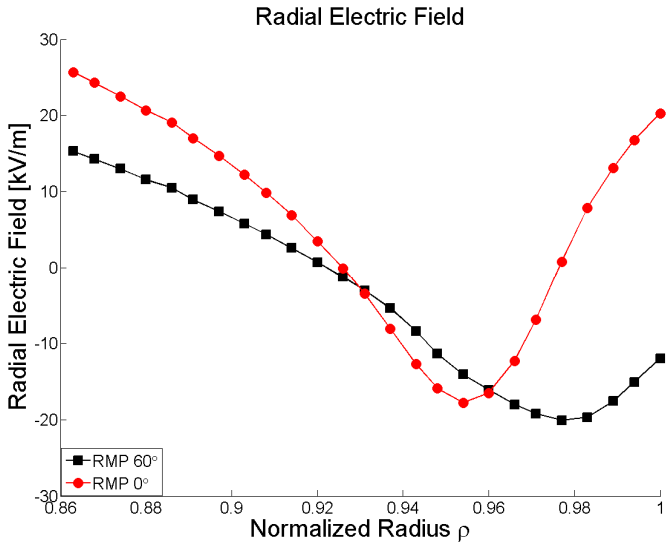

Figure 11: Measured radial electric field [kV/m] as a function of normalized radius.

The radial electric field for the I-coil phase 60° remains negative for ρ >0.93, while the 0° case becomes positive again just inside the separatrix at about ρ = 0.98. The sign change of the electric field between RMP phases will be shown to affect the particle pinch velocity and thus have an important effect on transport, and hence on the density profiles. Poloidal velocity profiles may also be affected by the radial electric field profiles shown in Fig. 11.

One major observation is the shift in location of the "well" between phase profiles. There is some uncertainty in determining the separatrix location, which introduces some uncertainty in abscissa which may differ for the two phases. Another possibility for this radial electric field shift between phases is attributed to data processing, where the boundary condition of the electron temperature is assumed to be 50 eV at a normalized flux surface equal to one. However, this shift was not applied to the ion profiles, therefore not affecting the velocity profiles from which this electric field is calculated. This electron shift is a common practice for diagnostics in tokamaks, but remains an issue to be examined in future analysis, causing possible errors in the alignment of profiles, such as the radial electric field.

When applying the momentum balance constraints in Eqs (5) and (6) for the deuterium ion, several parameters appear which are not directly measured. In the DIII-D tokamak, the carbon toroidal and poloidal velocities are measured, and the deuterium velocities must be calculated. The deuterium and carbon toroidal velocities are frequently found to be comparable, allowing a first order perturbation analysis (shown in Appendix B) to be used to obtain the toroidal velocity profile for deuterium [29].

$$V_{\phi D} = V_{\phi C} + \frac{\left(n_D e_D E_\phi^A + e_D B_\theta \Gamma_D + M_{\phi D}\right) - n_D \nu_{dD} V_{\phi C}}{n_D m_D (\nu_{DC} + \nu_{dD})} \qquad (8)$$

When addressing the poloidal deuterium velocities, perturbation analysis cannot be used due to the differences usually found between the calculated carbon and deuterium poloidal rotation profiles. However, Eq. (6) can again be rearranged, this time balancing the deuterium momentum, to obtain the poloidal velocity for deuterium [29].

$$V_{\theta D} = \frac{1}{B_\phi}\left(B_\theta V_{\phi D} + \frac{1}{n_D e_D}\frac{\partial p_D}{\partial r} - E_r\right) \tag{9}$$

Through particle and momuntum constraints, the poloidal and toroidal velocities for both carbon and deuterium have been determined, as well as the particle flux and radial electric field. Toroidal velocities for both carbon and deuterium are shown in Fig. 12.

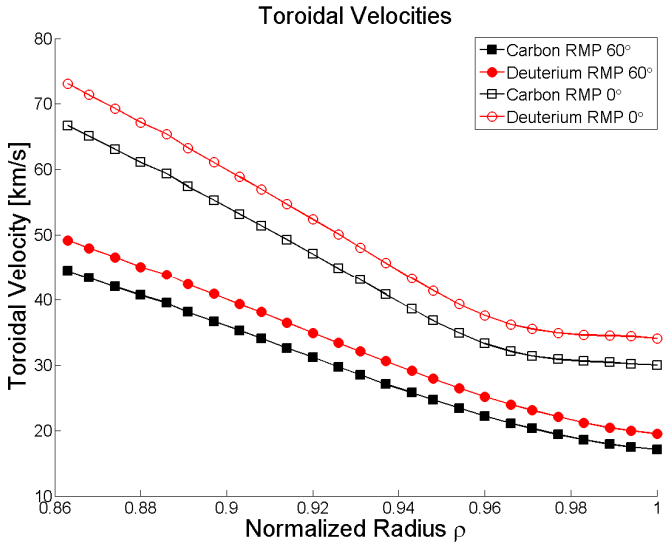

Figure. 12: Toroidal rotation velocities [km/s] for both measured carbon and calculated deuterium ions in the 0° and 60° phases.

An increase in both toroidal rotation velocity and its gradient can be seen for the 0° relative to the 60° phase in both the carbon and deuterium velocity profiles. Carbon and deuterium velocity profiles for both phases are similar enough to validate the use of perturbation theory shown in Eq. (8).

Poloidal rotation velocities, shown in Fig. 13, are similar between phases for $\rho < 0.96$. However, for $\rho > 0.96$, the poloidal rotation velocity is significantly larger for the 0° phase for both carbon and deuterium.

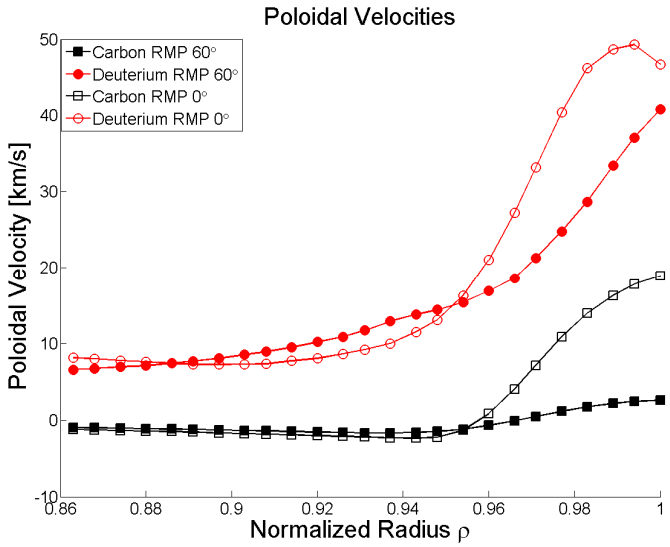

Figure 13: Poloidal rotation velocities for measured carbon and calculated deuterium ions for 0° and 60°.

CHAPTER 5

INFERRED PARTICLE TRANSPORT IN THE EDGE PEDESTAL

Momentum Transport Frequencies, Diffusion, and Non-Diffusive Particle Pinch

The toroidal momentum balance equation introduces momentum transport, or "drag", frequencies which are not directly measured quantities. Drag frequencies are denoted with a 'd' subscript, along with the designated ion subscript, and represent the momentum loss due to viscosity, charge exchange, inertia, and other "anomolous" forces [29]. The interspecies collision frequency is denoted by the subscript "DC", and accounts for the toroidal momentum transfer between deuterium and carbon. By using first order perturbation analysis of Eqs (5) and (6), expressions for these momentum transfer frequencies can be derived [29],

$$\nu_{dD} = \frac{\left(n_D e_D E_\phi^A + e_D B_\theta \Gamma_{rD} + M_{\phi D}\right) + \left(n_C e_C E_\phi^A + e_C B_\theta \Gamma_{\mathrm{rC}} + M_{\phi C}\right)}{(n_D m_D + n_C m_C) V_{\phi C}^{\exp}} \tag{10}$$

$$\nu_{dC} = \frac{(n_C e_C E_\phi^A + e_C B_\theta \Gamma_{\mathrm{rC}} + M_{\phi C}) + m_D n_D \nu_{DC} \left(V_{\phi D} - V_{\phi C}\right)_0}{n_C m_C V_{\phi C}^{exp}} \tag{11}$$

where the difference in toroidal velocity between the deuterium and the carbon is defined in the perturbation analysis above in Eq. (8). The deuterium drag frequencies and collision frequencies describing toroidal momentum transfer can be seen in Fig. 14, where it is shown that the momentum transport across flux surfaces by viscosity, charge exchantge, etc. dominates collisional momentum transfer between ion species. This shows that deuterium drag is the dominant mechanism for toroidal momentum transfer, and will subsequently be shown to influence radial diffusion.

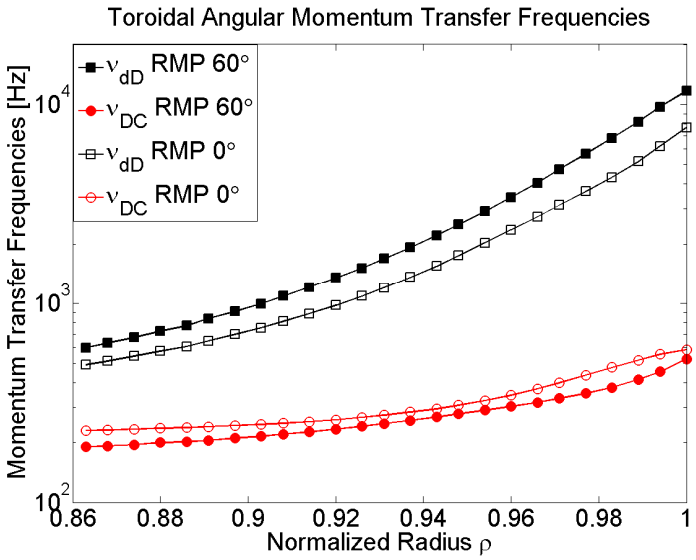

Figure 14: Calculated toroidal angular momentum transfer frequency ν_{dD} and interspecies collision frequency, ν_{DC}.

Continuing to rearrange these momentum balance equations, a pinch diffusion expression for the radial particle flux, Γ, can be obtained [29],

$$\Gamma_D = n_D V_D = -\frac{n_D D_D}{p_D}\frac{\partial p}{\partial r} + n_D V_{rD}^{pinch} \tag{12}$$

where the diffusion coefficient, D, is defined as [29]

$$D_D = \frac{m_D T_D \nu_{DC}}{(e_D B_\theta)^2}\left(1 + \frac{\nu_{dD}}{\nu_{DC}} - \frac{e_D}{e_C}\right) \tag{13}$$

and the pinch velocity is [29]

$$V_{rD}^{pinch} = \frac{\left[-M_{\phi D} - n_D e_D E_\phi^A + n_D m_D(\nu_{DC}+\nu_{dD})\left(\frac{B_\phi V_{\theta D}}{B_\theta} + \frac{E_r}{B_\theta}\right) - n_D m_D \nu_{DC} V_{\phi C}\right]}{n_D e_D B_\theta} \tag{14}$$

It is clear from Eq. (12) that the ion flux consists of a "standard" outward diffusive component from the pressure gradient (and therefore density and temperature gradients), as well as an inward non-diffusive, "pinch" term defined by Eq. (14).

Returning to Fig. 14, it is seen that deuterium drag frequencies for 60° are larger than for the 0° case, resulting in larger outward diffusion coefficients for the 60° case than for the 0° case, as shown in Fig. 15.

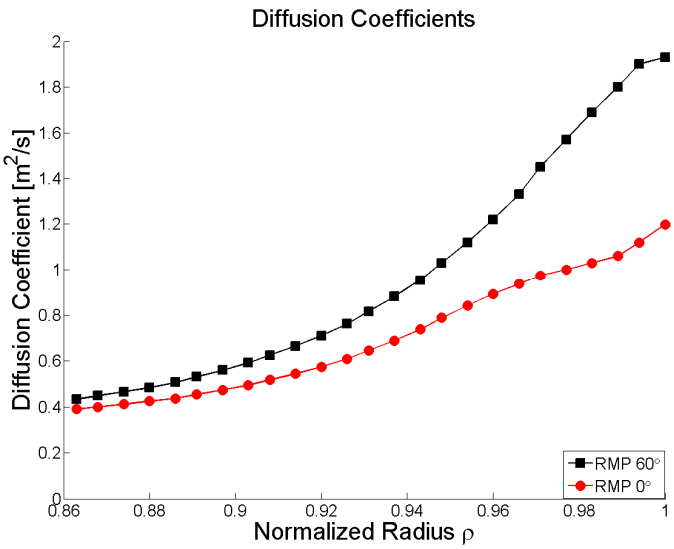

Figure 15: Calculated radially outward diffusion coefficients as a function of normalized radius.

The pinch velocity profiles, which are constructed using measured and calculated data to evaluate Eq. (14), become strongly negative (inward) in the plasma edge as shown in Fig. 16. Negative pinch velocities indicate an inward electromagnetic force and inward non-diffusive particle flux, which is somewhat stronger for the 60° phase than for the 0° phase.

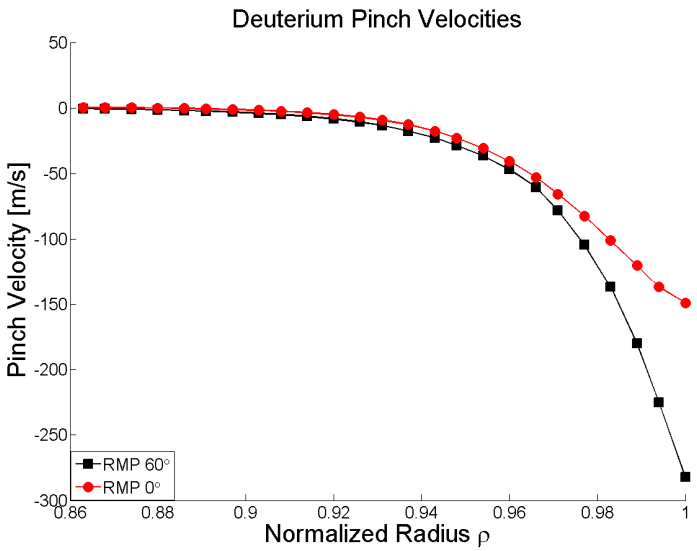

Figure 16: Calculated inward pinch velocity for 60° and 0°.

Momentum transfer frequencies, radial electric field, rotation velocities, as well as other factors all influence the pinch velocity profiles shown in Fig. 16. The decomposition of the dependence of the pinch velocity on each term in Eq. (14) can be seen for the 0° and 60° phases in Figs 17 and 18, respectively.

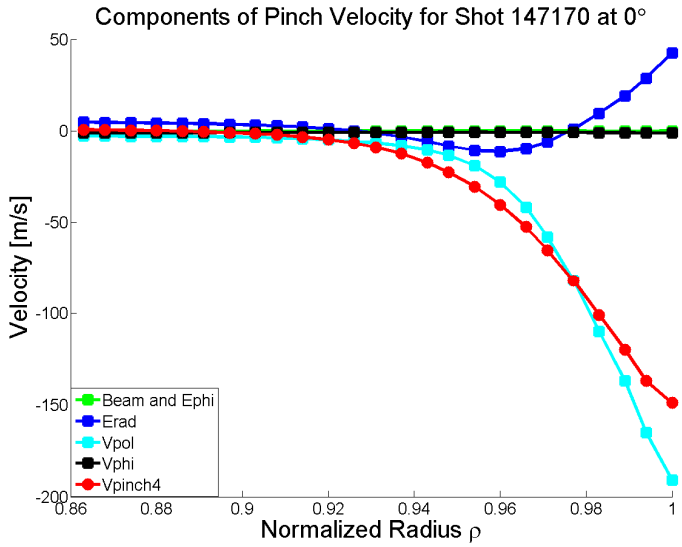

Figure 17: Decomposition of components of calculated Vpinch for 0° with terms depending on NBI and toriodal electric field, radial electric field, poloidal velocity, and toroidal velocity.

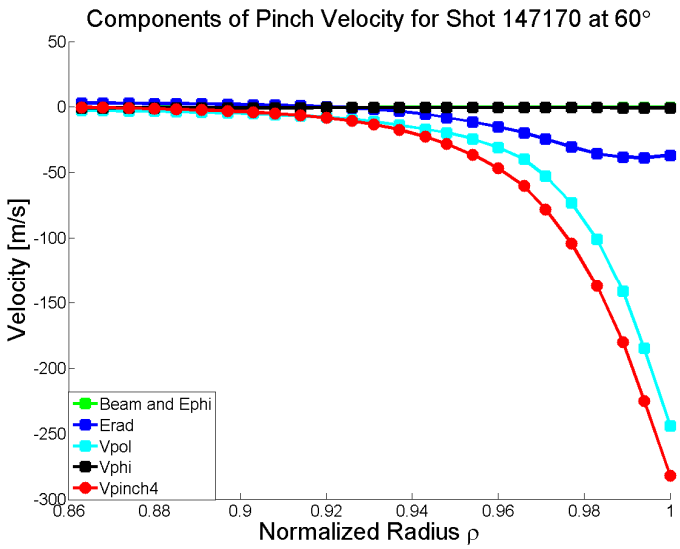

Figure 18: Decomposition of components of calculated Vpinch for 60° into terms depending on NBI and toriodal electric field, radial electric field, poloidal velocity, and toroidal velocity.

Poloidal velocity plays a key role in defining the pinch velocity for each phase, with a large negative Vpinch contribution for $\rho > 0.96$. This is the same region where the calculated poloidal velocity profile notably increased for deuterium ions in Fig. 13. The expression is negative due to the negative toroidal magnetic field shown in Appendix C Table C.1. The radial electric field component of the pinch velocity is the next most important term, enhancing the negative electric field component for the 60° phase and partially cancelling it for the for the 0° phase. These radial electric field contributions reflect the sign of the field profiles shown in Fig. 11.

The two major components of poloidal velocity and radial electric field are the only two terms that contain the toroidal drag frequency. Since the toroidal drag frequency dominates the collision frequency, the poloidal velocity and radial electric field terms are more important in the expression for pinch velocity. Since the 60° drag frequencies are

larger than those of 0°, it is expected that the pinch velocity will be larger, which is confirmed in Fig. 16.

Particle fluxes can be analyzed by looking at the diffusive components compared to the non-diffusive pinch components. The decomposition of particle fluxes in such a manner is shown in Fig. 19.

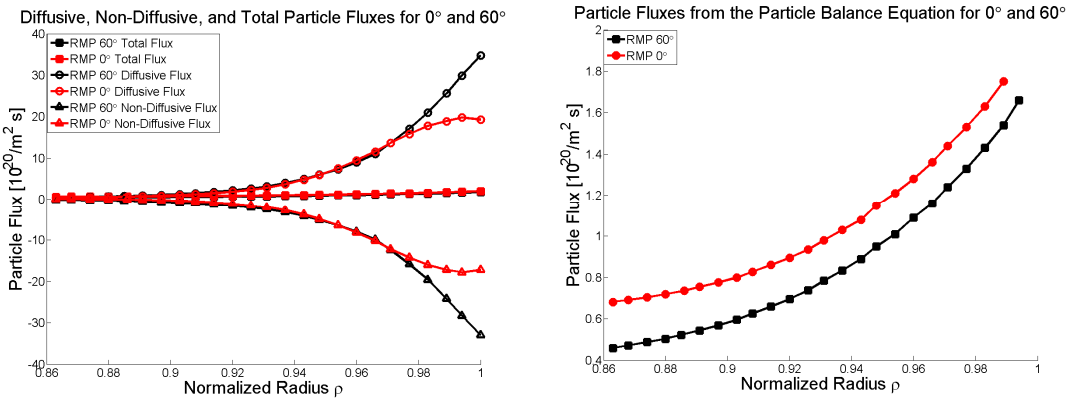

Figure 19: Calculated diffusive and non-diffusive pinch particle flux components of total flux and the net flux.

The larger diffusion coefficients for the 60° case than for the 0° case imply a larger outward diffusive flux for 60° than for 0°, which is consistent with the lower density profile for the 60° phase shown in Fig. 8. However, both the outward diffusive particle flux and the inward non-diffusive pinch transport are larger for the 60° phase, with values on the order of 30×10^{20} particles/m^{2}s. The net sum of the diffusive and non-diffusive fluxes yields a smaller total flux in the outward direction for the 60° case than for the 0° case on the order of 1×10^{20} particles/m^{2}s, which means that this cancellation could be sensitive to uncertainties in edge measurements. The larger cancellation of particle flux for 60° is associated with a lower edge pedestal density for 60° as compared to 0°. Understanding the underlying mechanisms which cause the pinch velocity and radial diffusion coefficient, such as the dependence on the toroidal angular momentum

transfer frequencies, is important for understanding how the RMP controls the edge density and thereby suppressing ELMs. In further studies, the drag frequencies may potentially be used to perturb the flux in a single direction and hence change the net particle flux.

Thermal Diffusivities from Conservation of Energy and Heat Conduction

Previous analysis has shown that pressure gradients for DIII-D RMP shots with n=3 I-coil perturbations have been reduced due to particle balance without an effective change in energy transport [7]. Thermal transport is an important part of plasma edge analysis and the formation of transport barriers, and therefore it is desirable to calculate thermal diffusivities. Plasma edge analysis is further constrained by conserving energy. The 2nd velocity moment of the Boltzmann equation is the conservation of energy for both the ions (D,C) and electrons (e) [29].

$$\frac{\partial Q_D}{\partial r} = -\frac{\partial}{\partial t}\left(\frac{3}{2} n_D T_D\right) + q_{nbD} - q_{De} - n_e n_0^c \langle \sigma v \rangle_{cx} \frac{3}{2}(T_D - T_0^c) \quad (15)$$

$$\frac{\partial Q_e}{\partial r} = -\frac{\partial}{\partial t}\left(\frac{3}{2} n_e T_e\right) + q_{nbe} + q_{De} - n_e n_C L_C(T_e) \quad (16)$$

Where, Q = q + (3/2) Γ T. The souce of ion energy is NBI or other external heating, and the sinks include collisions with electrons and charge exchange. The energy sources for electrons are external heating and the energy transferred from ions, while energy may be lost due to radiative cooling [29].

The 3rd velocity moment of the Boltzmann equation constrains heat conduction, however for simplicity, the familiar heat conduction relation shown in Eq. (17) is used in lieu of the complex third velocity moment equation.

$$q_{D,e} = -n_{D,e} \chi_{D,e} \frac{\partial \mathrm{T_{D,e}}}{\partial \mathrm{r}} \quad (17)$$

Using Eqs (15)-(17) to solve for the ion and electron heat fluxes and the calculated particle fluxes from the 0th moment constraint, the experimental heat diffusivities for both ions and electrons are inferred.

$$\chi_{D,e} = -\frac{Q_{D,e}^{exp} - \frac{3}{2}\Gamma_{D,e}^{exp} T_{D,e}^{exp}}{n_{D,e}^{exp}\left(\partial T_{D,e}^{exp} / \partial r\right)} \quad (18)$$

Inferred electron thermal diffusivities, as shown in Fig. 20, the strong dip in the pedestal region of the experimental diffusivity profiles implies the presence of an energy transport barrier around ρ > 0.96. This thermal transport barrier aligns with the pinch velocity inward electromagnetic force barrier discussed previously in Fig. 16.

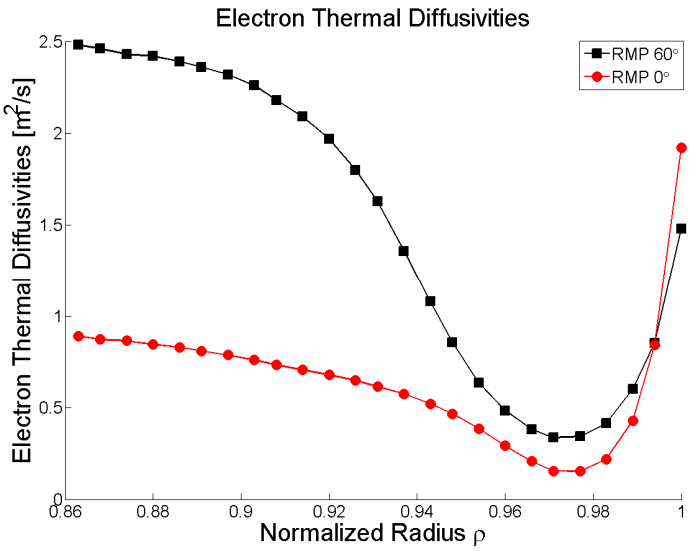

Figure 20: Inferred electron thermal diffusivities for 60° and 0°.

The electron thermal diffusivity is much larger in the flattop region for the 60° case, but the two phases have similar thermal diffusivities in the outer pedestal region. Ion thermal diffusivities, seen in Fig. 21, also show a trend for higher values for the 60° situation, however not with as great a difference as the electron diffusivities.

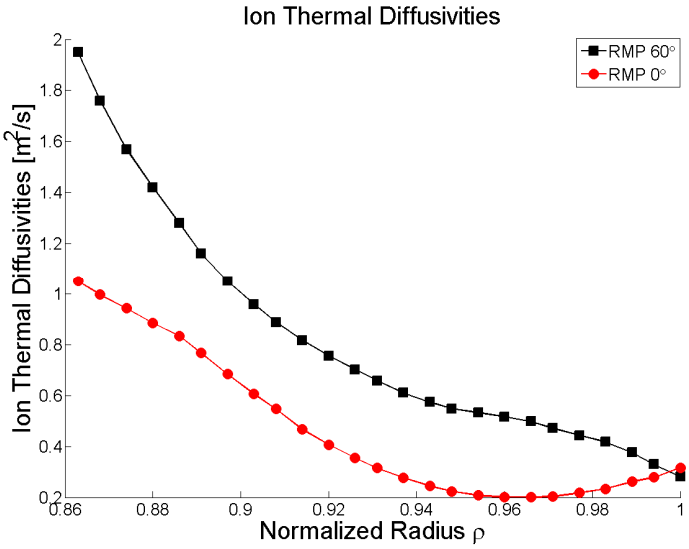

Figure 21: Inferred ion thermal diffusivities for 0° and 60° phases.

The constant decreasing thermal diffusivity trend does not suggest as much of an energy transport barrier for ions as did the electron thermal diffusivity profiles, especially for the 60° profile.

Ion Orbit Loss

Ion orbit loss is a mechanism that affects thermalized plasma ions, energetic neutral beam ions, and fusion alpha particles, causing them to travel across the last closed flux surface. These ions are assumed to be lost to the plasma and must be taken into account when interpretting measured data in terms of diffusive and non-diffusive transport processes taking place in the plasma.

Conservation of energy and canonical angular momentum can be used to derive a mimumum initial velocity, V_0, required for an ion to be lost across the last closed flux surface [30]. The mimumum velocity depends on the the initial location and direction of

the ion, the electrostatic potential, flux surface configuration, as well as other plasma parameters. This minimum velocity can be used to calculate the fraction of particles, momentum, and energy lost due to this ion orbit loss mechanism [30].

$$F_{orb} = \frac{N_{loss}}{N_{total}} = \frac{\int_{-1}^{1}[\int_{V_{0,\min}(\zeta_0)}^{\infty} V_0^2 f(V_0) dV_0]\, d\zeta_0}{2\int_0^{\infty} V_0^2 f(V_0) dV_0} \tag{19}$$

$$M_{orb} = \frac{M_{loss}}{M_{total}} = \frac{\int_{-1}^{1}[\int_{V_{0,\min}(\zeta_0)}^{\infty} (mV_0)\zeta_0 V_0^2 f(V_0) dV_0]\, d\zeta_0}{2\int_0^{\infty} (mV_0) V_0^2 f(V_0) dV_0} \tag{20}$$

$$E_{orb} = \frac{E_{loss}}{E_{total}} = \frac{\int_{-1}^{1}[\int_{V_{0,\min}(\zeta_0)}^{\infty} \left(\frac{1}{2}mV_0^2\right) V_0^2 f(V_0) dV_0]\, d\zeta_0}{2\int_0^{\infty} \left(\frac{1}{2}mV_0^2\right) V_0^2 f(V_0) dV_0} \tag{21}$$

Where ζ_0 is the cosine of the angle between the direction of the ion and the toroidal magnetic field. These expressions take into account all particles with energy above V_{0min}, travelling in all directions. Assuming a Maxwellian velocity distribution for all ions, the cumulative fractions of particles, momentum, and energy that are lost can be explicitly written as [30]

$$F_{orb} = \frac{\int_{-1}^{1} \Gamma\left(\frac{3}{2}, \epsilon_{0min}(\zeta_0)\right) d\zeta_0}{2\Gamma\left(\frac{3}{2}\right)} \tag{22}$$

$$M_{orb} = \frac{\int_{-1}^{1} \Gamma(2, \epsilon_{0min}(\zeta_0))\zeta_0 d\zeta_0}{2\Gamma(2)} \tag{23}$$

$$E_{orb} = \frac{\int_{-1}^{1} \Gamma\left(\frac{5}{2}, \epsilon_{0min}(\zeta_0)\right) d\zeta_0}{2\Gamma\left(\frac{5}{2}\right)} \tag{24}$$

where $\varepsilon_0 = mV_0^2/2kT$, $\Gamma(n)$ is the gamma function of order n, and $\Gamma(n, \varepsilon_0)$ is the incomplete gamma function of order n. The particle and energy loss fractions, shown in Figs. 22 and 23, are slightly higher for the 0° case for $\rho > 0.96$. Ion orbit momentum loss is also larger for the 0° phase, as seen in Fig. 24.

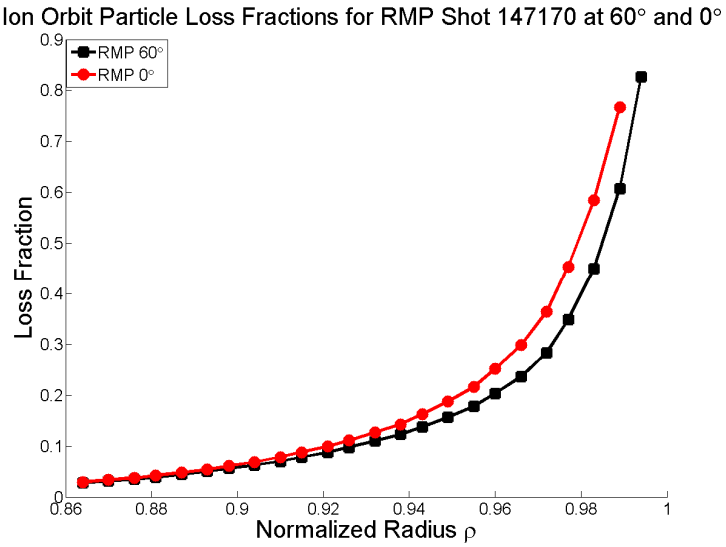

Figure 22: Calculated cumulative fraction of particles lost in the edge.

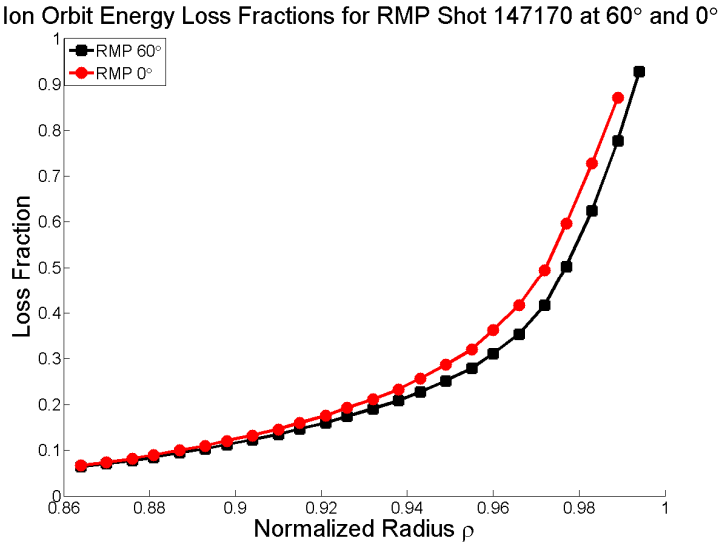

Figure 23: Calculated cumulative fraction of energy lost in the edge.

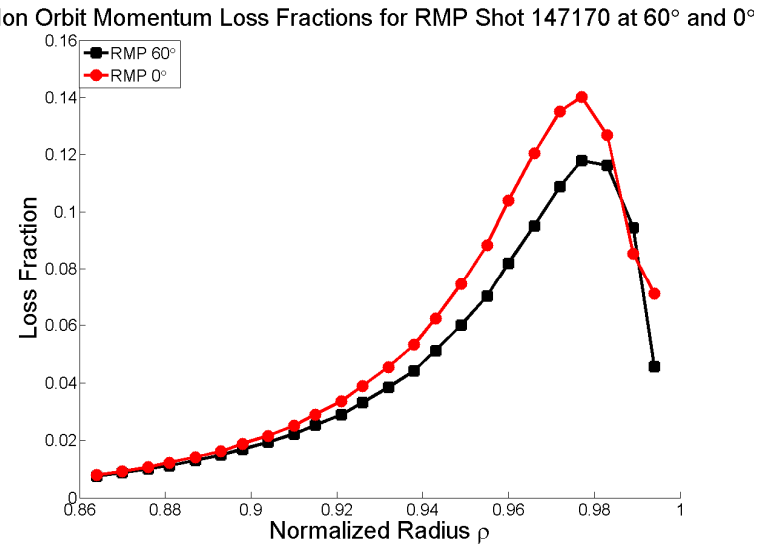

Figure 24: Calculated cumulative fraction of momentum lost in the edge.

The particle and energy loss fractions are significant and must be accounted for in various profiles such as the particle flux and thermal diffusivities, which have thus been reported in the present work without the ion orbit loss correction. The particle and energy orbit loss fractions do not vary significantly between phases; however, the difference between momentum loss fractions between phases is notable in the region identified as the transport barrier.

Particle loss fractions are applied to correct the original particle balance in Eq. (3)

$$\Gamma_{orb} = (1 - F_{orb})\Gamma = (1 - F_{orb})n_D v_D \tag{25}$$

which now does not include lost particles in the transport particle flux used in the interpretation of transport. The ion orbit modified flux is compared to the unaltered flux from the continuity equation in Fig. 25.

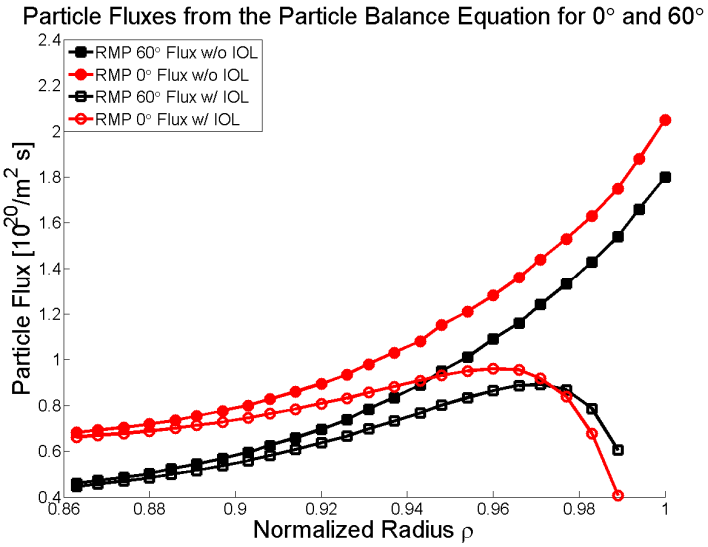

Figure 25: Calculated particle flux for 0° and 60° phases with and without the ion orbit loss correction.

With this correction to the flux, it can be seen that the 0° flux drops below the 60° flux in the pedestal region. The transport of particles, as distinguished from the outflux of particles due to transport plus ion orbit loss, is clearly seen to be drastically reduced in both phases for $\rho > 0.96$. The reduction is greater for the 0° phase, which is consistent with the observation of larger edge particle density for this phase. This was not apparent before the ion orbit loss correction was applied.

A similar procedure can be used to modify the inferred heat diffusivities.

$$\chi_{orb} = -\frac{(1-E_{orb})Q_{exp}-\frac{3}{2}\Gamma^{exp}(1-F_{orb})T^{exp}}{n^{exp}\left(\partial T^{exp}/\partial r\right)} \tag{26}$$

The impact of ion orbit loss on electron thermal diffusivities is seen in Fig. 26 to have a small effect on the inerred energy transport for the electrons. The ion orbit loss actually increases the profile slightly, but has no major significance in the interpretive outcome when comparing the dependence on toroidal phase. The 0° phase profile still takes on a value over twice that of the 60° phase in the flattop region, and the two profiles become comparable at the thermal transport barrier around $\rho = 0.96$-0.98 as before.

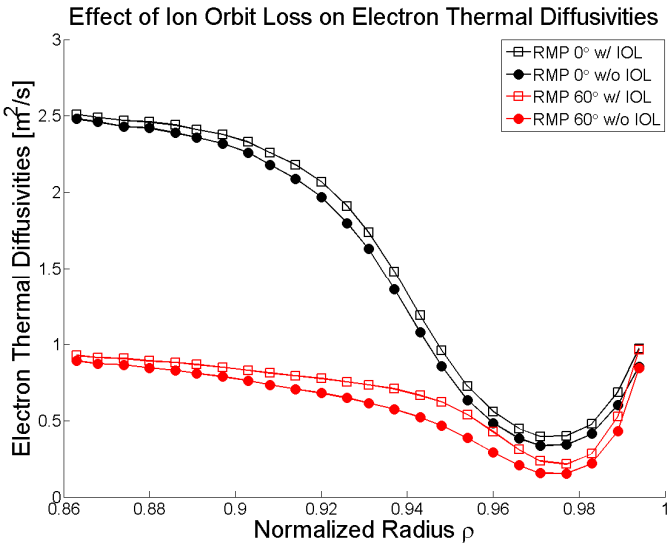

Figure 26: Calculated electron thermal diffusivities for the 0° and 60° phases with and without the ion orbit loss correction.

The ion orbit loss correction can also be applied to the ion diffusivities in the same manner. Effects of this correction are seen in Fig. 27.

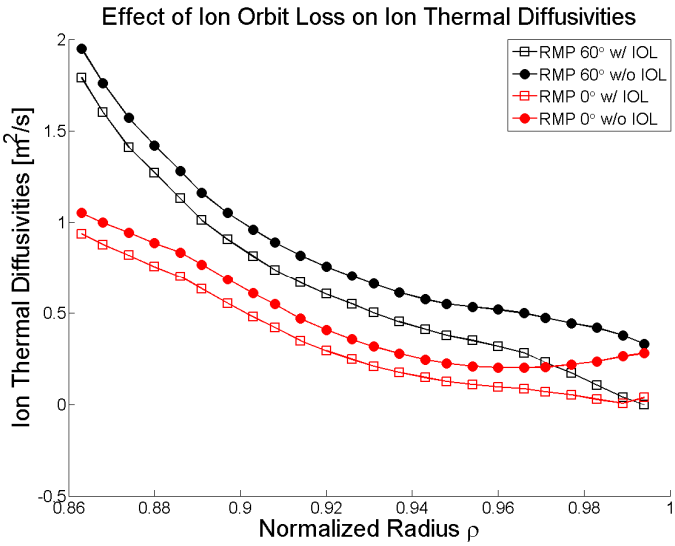

Figure 27: Calculated ion thermal diffusivities for the 0° and 60° phases with and without the ion orbit loss correction.

Ion orbit loss effects the ion thermal diffusivities in the opposite manner than the electrons by decreasing the profile. Toroidal phase has a limited effect on the ion

diffusivity profiles, especially in the pedestal region, which is consistent with the paradigm that RMPs suppress ELMs without significantly changing thermal transport [7].

Intrinsic Rotation

When analyzing ion orbit momentum loss, it has been recognized [31, 32] that momentum loss in the edge occurs in a preferential direction, usually counter-current for anti-parallel toroidal current and magnetic field, leaving more particles in the plasma with co-current rotation velocities. A counter-current sink in momentum appears as an increase in intrinsic co-current rotation in the plasma edge. An expression for the increase in toroidal rotation velocity can be shown to be [31]

$$\Delta V_\phi = 2\frac{\Gamma(2)}{\sqrt{\pi}} M_{orb}(\rho) V_{th}(\rho) \tag{27}$$

Where Γ is the gamma function, and V_{th} is the ion thermal velocity. Intrinsic rotation, shown in Fig. 28, is induced more for 0° because the momentum loss fraction is larger while the ion temperatures are kept fairly constant.

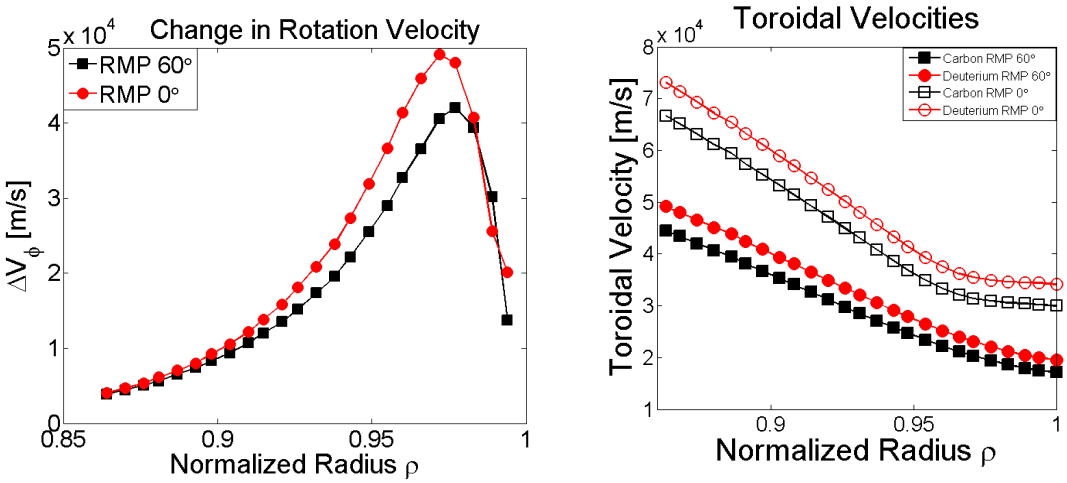

Figure 28: Calculated change in toroidal rotation velocity due to ion orbit loss and measured toroidal velocities.

The increase in toroidal velocity for 0° is roughly $1x10^4$ m/s from Fig. 12, implying that RMPs may cause intrinsic rotation in tokamaks. Intrinsic rotation is desirable for the stabilization of Resistive Wall Modes without externally injected torque. The calculated intrinsic toroidal velocity for the 0° case is roughly $1x10^4$ m/s in the pedestal region, which is consistent with the difference in measured toroidal velocity between phases. This is suggestive that ion orbit loss could be causal for the observed differences in toroidal velocity between the two phases, and perhaps controllable if better understood. However, there may be other mechanisms, such as $\vec{j} \times \vec{B}$ torque from the radial magnetic field perturbation, that are more dominant.

Consistency Check for Pinch Diffusion

As a consistency check, a comparison is made between the radial ion particle fluxes calculated using the experimental data to solve the continuity equation of Eq. (3) with those obtained by using the experimental and calculated data to evaluate the pinch diffusion relation of Eq. (12). These fluxes, with and without corrections for ion orbit loss [30], are shown in Figs. 29 and 30.

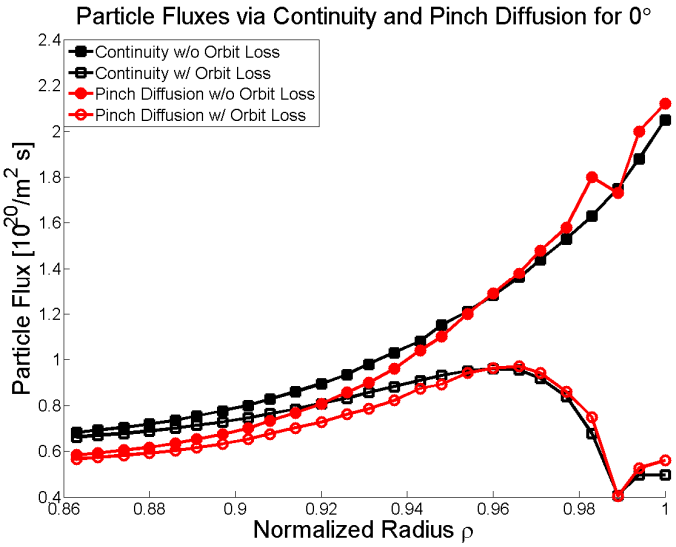

Figure 29: Comparison of particle fluxes with and without orbit loss calculated via the continuity equation and the pinch diffusion relation for 0°.

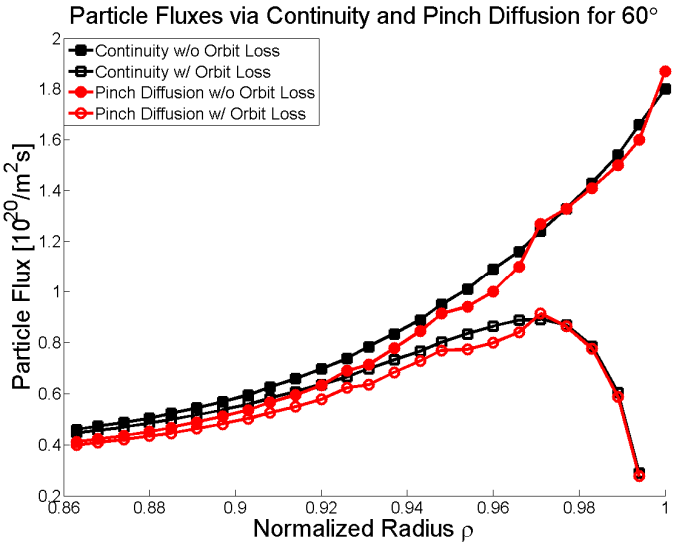

Figure 30: Comparison of particle fluxes with and without orbit loss calculated via the continuity equation and the pinch diffusion relation for 60°.

It is clear that there is agreement between the two calculations of flux, and for each phase the average error is within 8.5%, with the largest error being just under 15% at the beginning of the profiles most likely due to boudary condition constraints used in the calculation.

CHAPTER 6

CONCLUSIONS

Repeated reversals of resonant magnetic perturbations of the I-coil between 0° and 60° toroidal phases in DIII-D shot 147170 generate different edge pedestal profiles. Measured density, temperature, and rotation profile variations can be interpreted as differences in diffusive and non-diffusive transport, resulting in a theoretical basis for a better understanding of RMP toroidal phase effects on pedestal transport.

Large outward diffusive particle fluxes and comparably large inward electromagnetic particle pinches are found for both RMP toroidal phases. The opposing fluxes compensate each other and produce a net outward particle flux smaller than its diffusive and non-diffusive components by an order of magnitude. The net outward particle flux is found to be larger for the 0^o than for the 60^o RMP phase, agreeing with the larger density for 0°. The 60° phase has a larger flux balance, however, with both the diffusive and non-diffusive flux components larger than in the 0° phase. The particle fluxes found from evaluating the pinch-diffusion relation using experimental data agree with the fluxes obtained by solving the continuity equation for both toroidal RMP phases, confirming the internal consistency of this analysis.

Electron and ion thermal diffusivities inferred from the density and temperature profiles are similar for the two toroidal phases in the steep-gradient pedestal region, but differ in the flattop region further inward, where the 60° phase is larger than the 0° phase for both species. The electron thermal diffusivity profiles exhibited a “transport barrier” well just inside the separatrix.

Toroidal momentum transport frequencies, or "drag" frequencies, are larger than interspecies collision frequencies, and had a major effect on both the diffusive and non-diffusive transport. The 60° phase had larger "drag" frequencies, which appeared to be the driving factor for the increased flux components for this phase. This would imply that one mechanism by which RMP affects edge transport is through exerting a torque on the edge plasma.

By interpreting the density and rotation velocity profiles, an argument can be made that the increased density for the 0° toroidal phase relative to the 60^{o} phase may be ultimately driven by the larger intrinsic rotation velocity attributable to ion orbit loss. The larger toroidal velocity for 0° leads to an inference of smaller momentum transport "drag" frequencies, which in turn is interpreted as smaller particle diffusion coefficients by using the momentum balance constraint. The smaller diffusion coefficients for 0° lead to fewer particles leaving the plasma via diffusive processes for 0° than 60°. Diffusion plays a key role determining the edge pedestal density profiles for each toroidal phase in conjunction with the non-diffusive pinch velocities. Other plausible explanations which have not been examined in this work, such as the $\vec{\boldsymbol{j}} \times \vec{\boldsymbol{B}}$ torque from radial currents and the non-axisymmetry of the "background" or "error" radial magnetic field, may also play a role in driving intrinsic rotation.

Future work includes applying the present analysis to a similar RMP shot in DIII-D with a nulled out interference, or n=0, in the RMP fields between toroidal phases to determine if similar trends occur.

APPENDIX A

THE BOLTZMANN EQUATION AND ITS MOMENTS

The particle balance equation shown in Eq. (A.1) can be defined for every particle in all regions of the plasma to determine the position and velocity distributions of tokamak plasmas [28].

$$\frac{dF_N}{dt}(x_1, \dots, x_N, v_1, \dots, v_N, t) = C_N(x_1, \dots, x_N, v_1, \dots, v_N, t) + S_N(x_1, \dots, x_N, v_1, \dots, v_N, t) \quad \text{(A.1)}$$

Here, F is the distribution function, where the total time rate of change of particles in a differential position and velocity phase space volume is equal to the rate of sources minus sinks due to particles scattering into or out of other spatial-velocity phase space volumes. F_1 describes the probability of particle 1 being in a volume element of Δx_1 with velocity within the element Δv_1 at time t. This function can then be defined for all N particles. The first term on the right hand side, C_N, is the collision term that takes into account the changes in the particle distribution function due to collisions, resonant interactions with electromagnetic waves, as well as other interactions on the same time scale. S_N is the source term that considers all other particle sources and sinks. The total time derivative can be expressed as [28]

$$\frac{dF_N}{dt} = \frac{\partial F}{\partial t} + \sum_{j=1}^{N} \boldsymbol{v}_j \cdot \nabla_j F_N + \sum_{j=1}^{N} \boldsymbol{a}_j \cdot \nabla_{vj} F_N = C_N + S_N \quad \text{(A.2)}$$

where all the collective particle interactions, such as those concerned with electromagnetic forces, are included in the distribution function and not the collision or source terms. The velocity derivative, or acceleration, can then be expressed in terms of

the electric and Lorentz forces [28] yielding Eq. (A.3), which is known as the Boltzmann equation and can be applied to each particle species in the plasma.

$$\frac{\partial \boldsymbol{f}}{\partial t} + \boldsymbol{v} \cdot \nabla f + (\boldsymbol{E} + \boldsymbol{v} \times \boldsymbol{B}) \cdot \nabla_v f \equiv \boldsymbol{C} + \boldsymbol{S} \tag{A.3}$$

However, kinetic treatment of the plasma is rigorous, and to avoid excessive computation time for the large amounts of particles present inside tokamaks, the plasma can be treated as a fluid by applying velocity moments to the Boltzmann equation in Eq. (A.3) to obtain classical balance equations of continuity, momentum, and energy. The 3rd velocity of the Boltzmann equation is highly complex, and therefore the familiar heat conductivity equation is used to close the system.

The 0th velocity moment of Eq. (A.3) is taken by multiplying the entire equation by 1 and integrating over all possible velocities, and is described by Eq. (A.4), which represents continuity of particles.

$$\frac{\partial n}{\partial t} + \nabla \cdot n\boldsymbol{v} = \boldsymbol{S}^0 \tag{A.4}$$

The continuity equation can be solved for the particle density from the external sources in the S^0 term comprised of ionization sources as well as external particle sources such as neutral beam injection (NBI). The simplification of Eq. (A.3) to Eq. (A.4) can be made with the following definitions for particle density and average fluid velocity:

$$n = \int f(v) d^3 v \tag{A.5}$$

$$\boldsymbol{v} = \frac{\int f(\boldsymbol{v}) \boldsymbol{v} d^3 \boldsymbol{v}}{n} \tag{A.6}$$

By assuming a steady state plasma, this continuity equation directly yields the particle flux by integrating the source term over the plasma edge, which was the process used in the present work.

The 1st velocity moment of Eq. (A.3) is obtained by multiplying the entire equation by '$m\mathbf{v}$' and integrating over all possible velocities, generating an equation that represents a momentum balance for the plasma species on which it is applied.

$$m\frac{\partial(nv)}{\partial t} + \nabla \cdot \boldsymbol{M} - ne(\boldsymbol{E} + \boldsymbol{v} \times \boldsymbol{B}) = \boldsymbol{R^1} + \boldsymbol{S^1} \tag{A.7}$$

Here, M is the momentum stress tensor defined as

$$\boldsymbol{M} \equiv nm(\boldsymbol{vv}) \tag{A.8}$$

and R^1 is the collision term due to friction

$$\boldsymbol{R^1} \equiv \int \boldsymbol{C}\, m\boldsymbol{v}\, d^3\boldsymbol{v} \tag{A.9}$$

and S^1 is the 1st velocity moment of the source term in Eq. (A.3). The momentum stress tensor can be decomposed into thermal and non-thermal motions and the gradient can be thought of as a volumetric momentum rate, or streaming of momentum.

The 2nd velocity moment of the Boltzmann equation yields an energy balance. This equation is constructed by multiplying Eq. (A.3) by '$\frac{1}{2}m(\mathbf{v}\cdot\mathbf{v})$' and integrating over all possible velocities to obtain Eq. (A.10) [28].

$$\frac{1}{2}\frac{\partial}{\partial t}(TrM) + \nabla \cdot \boldsymbol{Q} = ne\boldsymbol{v} \cdot \boldsymbol{E} + \boldsymbol{R^2} + \boldsymbol{S^2} \tag{A.10}$$

Here, TrM is the scalar Trace of tensor M, which can be represented by [28]

$$TrM = nm(\boldsymbol{v} \cdot \boldsymbol{v}) \tag{A.11}$$

Which represents an infinitesimal change in volume, or essentially the derivative of the determinant of the tensor M brought forth by the chain rule. The value Q is the energy flow for all particles of the species to which the energy balance is applied and is defined as [28]

$$Q = \frac{1}{2}nm(\boldsymbol{v} \cdot \boldsymbol{v})\boldsymbol{v} \tag{A.12}$$

which is matrix form of the kinetic energy flow of the plasma particles. The magnetic field term disappears with this integral leaving only the electric field term with the 2nd moment of both the collision and source terms.

The 3rd velocity moment of the Boltzmann equation represents an energy flux balance and is constructed by multiplying Eq. (A.3) by '$\frac{1}{2}\mathrm{m}(\mathbf{v}\cdot\mathbf{v})\mathbf{v}$' and integrating over all possible velocities to obtain Eq. (A.13) [28].

$$\frac{\partial \mathbf{Q}}{\partial \mathrm{t}} + \nabla\cdot\boldsymbol{\theta} - \frac{1}{2}\frac{\mathrm{e}}{\mathrm{m}}(\mathrm{TrM})\mathbf{E} - \frac{\mathrm{e}}{\mathrm{m}}\mathbf{M}\cdot\mathbf{E} - \frac{\mathrm{e}}{\mathrm{m}}\mathbf{Q}\times\mathbf{B} = \mathbf{R^3} + \mathbf{S^3} \tag{A.13}$$

Here, the $\boldsymbol{\theta}$ matrix is the energy flux tensor described by [28]

$$\theta = \frac{1}{2}\mathrm{nm}(\mathbf{v}\cdot\mathbf{v})\mathbf{v}\mathbf{v} \tag{A.14}$$

and is a new unknown generated by this moment equation. In order to close the set of equations and avoid using this detailed energy flux moment, the familiar heat conduction equation is used in lieu of Eq. (A.13),

$$\mathrm{q} = -\mathrm{n}\chi\frac{\partial \mathrm{T}}{\partial \mathrm{r}} \tag{A.15}$$

which is justified by the fact that Eq. (A.15) is obtained when simplifying the 3rd velocity moment in Eq. (A.13) to leading order under regular tokamak plasma conditions. This set of closed equations can be used to interpret plasma characteristics as set forth in the present work.

APPENDIX B

1ST ORDER PERTURBATION THEORY CALCULATION OF DEUTERIUM TOROIDAL VELOCITY

First order perturbation theory is used to calculate the deuterium toroidal rotation velocities from the measured carbon impurity ion toroidal velocities. The flux surface averaged toroidal angular momentum constraint calculated from plasma fluid theory for ion species j is underlying balance used for this calculation.

$$n_j m_j\left[\nu_{jk}\left(v_{\phi j} - v_{\phi k}\right) + \nu_{dj} v_{\phi j}\right] = n_j e_j E_\phi^A + e_j B_\theta \Gamma_{rj} + M_{\phi j} \tag{B.1}$$

This momentum balance equation introduces "drag" frequencies, ν_{dj}, that take into account momentum loss due to viscosity, charge exchange, inertia, and other anomalous processes. E^A is the electromagnetically induced toroidal electric field, and M_Φ is the toroidal component of the momentum input [33]. The quantities on the right hand side of Eq. (B.1) are generally known by direct measurements or calculations from measurements such as the radial flux. The momentum transfer frequencies can be calculated as long as the temperature and density profiles are known in the edge. By summing Eq. (B.1) of ion species j with that of ion species k, Eq. (B.2) may be obtained.

$$n_j m_j[\nu_{jk}\left(v_{\phi j} - v_{\phi k}\right) + \nu_{dj} v_{\phi j}] + n_k m_k[\nu_{kj}\left(v_{\phi k} - v_{\phi j}\right) + \nu_{dk} v_{\phi k}] = E_\phi^A\left(n_j e_j + n_k e_k\right) + B_\theta\left(e_j \Gamma_{rj} + e_k \Gamma_{rk}\right) + M_\phi \tag{B.2}$$

Here, M_Φ is the total toroidal momentum input for all species. The two drag frequency terms can be combined by defining an effective momentum transfer frequency shown in Eq. (B.3).

$$\nu_d^{eff} \equiv \frac{n_j m_j \nu_{dj} + n_k m_k \nu_{dk}}{n_j m_j + n_k m_k} = \frac{(n_j e_j E_\phi^A + e_j B_\theta \Gamma_{rj} + M_{\phi j}) + (n_k e_k E_\phi^A + e_k B_\theta \Gamma_{rk} + M_{\phi k}) - \{n_j m_j \nu_{dj}(v_{\phi j} - v_{\phi k})\}}{(n_j m_j + n_k m_k) v_{\phi k}} \tag{B.3}$$

A 0^{th} order approximation can be made by setting the term with the difference of toroidal velocities for each species equal to zero. This zeroth order approximation of the drag frequency can then be written as

$$\nu_d^0 = \frac{(n_j e_j E_\phi^A + e_j B_\theta \Gamma_{rj} + M_{\phi j}) + (n_k e_k E_\phi^A + e_k B_\theta \Gamma_{rk} + M_{\phi k})}{(n_j m_j + n_k m_k) v_{\phi k}} \tag{B.4}$$

which can be used in the toroidal momentum balance equation in Eq. (B.1) along with the experimentally measured carbon impurity toroidal velocity to determine the zeroth order difference between the carbon and deuterium toroidal velocities.

$$(v_{\phi j} - v_{\phi k})_0 = \frac{(n_j e_j E_\phi^A + e_j B_\theta \Gamma_{rj} + M_{\phi j}) - n_j m_j \nu_d^0 v_{\phi k}^{exp}}{n_j m_j (\nu_{jk} - \nu_d^0)} \tag{B.5}$$

Assuming that the effective momentum transport frequency is about the same as the deuterium drag frequency, this expression can be plugged back into the original toroidal angular momentum conservation equation in Eq. (B.1), but this time applied to the carbon ion to yield an expression for the carbon momentum transfer frequency [33].

$$\nu_{dk} = \frac{(n_k e_k E_\phi^A + e_k B_\theta \Gamma_{rk} + M_{\phi k}) + n_k m_k \nu_{kj} (v_{\phi j} - v_{\phi k})_0}{n_k m_k v_{\phi k}^{exp}} \tag{B.6}$$

APPENDIX C

EXPERIMENTAL DATA OBTAINED FROM THE DIII-D DATABASE USED AS INPUT INTO GTEDGE

Data obtained from EFITools in the DIII-D database for both 0° and 60° time slices are defined in Table C.1, with the variable names corresponding to the input value to GTEDGE and not necessarily the variable name in the EFITools plasma equilibrium GUI. The 0° time slice was obtained from the 3371.117ms EFIT3 measurement for shot 147170 and the 60° time slice was obtained from the 3151.117ms EFIT3 measurement.

Table C.1: Data from EFITools in the DIII-D database.

Parameter	Description	3371.117ms - 0°	3151.117ms - 60°
rmajor [m]	Major Radius	1.744	1.739
aminor [m]	Minor Radius	0.599	0.599
elong	Elongation	1.804	1.803
triang	Lower Triangularity	0.632	0.647
plasmacur [MA]	Plasma Current	1.612	1.608
B [T]	Magnitude of Toroidal Magnetic Field	1.947	1.948
bphi [T]	Vector Toroidal Magnetic Field	-1.947	-1.948
q95	Safety Factor at 95% flux surface	3.401	3.394
rx [m]	Radial coordinate of x-point	1.308	1.298
zx [m]	Axial coordinate of x-point	-1.231	-1.237
rsep1 [m]	Radial coordinate of the Outboard separatrix	1.372	1.364
rsep2 [m]	Radial coordinate of the Inboard separatrix	1.106	1.109
zsep1 [m]	Axial coordinate of the Outboard separatrix	-1.363	-1.363
zsep2 [m]	Axial coordinate of the Inboard separatrix	-1.315	-1.318
ssi95	Magnetic shear	4.485	4.314
pohmin [MW]	Minimum ohmic heating power	0.303	1.613

GTEDGE model parameters were adjusted in order to balance the background plasma. Table C.2 displays the values which matched the calculated and experimentally measured line average densities, energy confinement times, and central and pedestal temperatures.

Table C.2: GTEDGE model parameters that balanced the background plasma for each toroidal phase.

Parameter	Type	3371.117ms - 0°	3151.117ms - 60°
Nev2	Balanced	0.4039 E20	0.3705 E20
tauE	Balanced	0.3107	0.163
Central Temp	Balanced	6000	5574
Pedestal Temp	Balanced	1309	1316
Cballoon	Model	38.7	64.5
Hconf	Model	2.82	1.43
Tauratio	Model	0.5	0.5
Hrat	Model	0.39	1.2
Alphan	Model	-2.935	-2.513
Delxpt	Model	0.1	0.1
Delxreal	Model	0.05	0.05

Other calculated parameters from the experimental data that were used as direct inputs into GTEDGE are shown in Table C.3. Data not listed but gathered from the DIII-D database as an input to GTEDGE includes radial profiles in the edge at 25 discrete points for toroidal velocity, toroidal velocity gradient scale length, poloidal velocity, radial electric field, qedge, electron temperature gradient scale length, electron temperature, ion temperature gradient scale length, ion temperature, electron density, and electron density gradient scale length.

Table C.3: Experimentally calculated values input into GTEDGE.

Parameter	Description	3371.117ms - 0°	3151.117ms - 60°
xnpedex	Experimental Density at Pedestal	3.112E19	2.375E19
xnsepex	Experimental Density at Separatrix	0.319E19	0.175E19
tpedexi	Experimental Ion Temperature at Pedestal	1531.2	1656
tsepexi	Experimental Ion Temperature at Separatrix	343.7	375
tpedexe	Experimental Electron Temperature at Pedestal	1087.5	975
tsepexe	Experimental Electron Temperature at Separatrix	37.5	37.5
widthnx	Width of Density Pedestal→Separatrix	0.106	0.089
widthtex	Width of Electron Temperature Pedestal→Separatrix	0.082	0.063
widthtix	Width of Ion Temperature Pedestal→Separatrix	0.063	0.048
gradnbar	Density Gradient Scale Length	0.065	0.052
gradTbar	Average Temperature Gradient Scale Length	0.05	0.038
gradTebar	Electron Temperature Gradient Scale Length	0.044	0.034
aped	Ratio of Pedestal Density to Average Density	7.7	6.41
xnctrped	Ratio of Central Density to Pedestal Density	1.81	2.4
tctrped	Ratio of Center Temperature to Average Pedestal Density	4.58	4.24

REFERENCES

1. W. M. Stacey, *Fusion: An Introduction to the Physics and Technology of Magnetic Confinement Fusion*. 2010: WILEY-VCH GmbH & Co, KGaA, Weinheim.
2. T. E. Evans, *Chaos, Complexity and Transport: Theory and Applciations, "Implications of topological complexity and hamiltonian chaos in the edge magnetic field of toroidal fusion plasmas"*, ed. Cristel Chandre, Xavier Leoncini, and George Zaslavsky. 2008: Scientific World Press.
3. W. M. Stacey, *Ion particle transport in the tokamak edge plasma.* Contrib. Plasma Phys., 2008. **48**(1-3): p. 94-98.
4. F. Wagner et al., *Regime of Improved Confinement and High Beta in. Neutral-Beam-Heated Divertor Discharges of the ASDEX Tokamak.* Physical Review Letters, 1982. **49**(19): p. 1408-1412.
5. H. Zohm, *Edge localized modes (ELMs).* Plasma Phys. Control. Fusion, 1996. **38**: p. 105-128.
6. K. H. Burrell et al., *ELM suppression in low edge collisionality H-mode discharges using n=3 magnetic perturbations.* Plasma Phys. Control. Fusion, 2005. **47**: p. B37-B52.
7. T. E. Evans et al., *Edge stability and transport control with resonant magnetic perturbations in collisionless tokamak plasmas.* Nature (2006) 419.
8. W. M. Stacey and T. E. Evans, *The Role of Radial Particle Pinches in ELM Suppression by Resonant Magnetic Perturbations.* Nuclear Fusion, 2011. **51**(013007).
9. E. Nardon et al., *Edge localized mode control by resonant magnetic perturbations.* J. Nucl. Mater. 363-365 (2007) 1071.
10. T. E. Evans et al., *Suppression of large edge localized modes with edge resonant magnetic fields in high confinement DIII-D plasmas.* Nuclear Fusion, 2005. **45**: p. 595-607.
11. P. Gohil et al., *Control of plasma profiles in DIII-D discharges.* Plasma Phys. Control. Fusion, 2006. **48**: p. A45-A53.
12. B. Hudson, T. E. Evans, C. Petty, and P. Snyder, *Dependence of resonant magnetic perturbation experiments on the DIII-D plasma shape.* Nuclear Fusion, 2010. **50**(064005).
13. T. E. Evans et al., *RMP ELM suppression in DIII-D plasmas with ITER similar shapes and collisionalities.* Nuclear Fusion, 2008. **48**(024002).
14. T. E. Evans et al., *Suppression of large edge localized modes in high confinement DIII-D plasmas with a stochastic magnetic boundary.* J. Nucl. Mater. 337-339 (2005) 691.
15. J. D. Callen, A. J. Cole, and C.C. Hegna, *Toroidal rotation in tokamak plasmas*, in *22nd Annual IAEA Fusion Energy Conference*2009, International Atomic Energy Agency: Geneva, Switzerland. p. IAEA-CN-165/TH/P8–36.
16. L. Frassinetti, S. Menmuir, K. E. J. Olofsson, P. R. Brunsell, and J. R. Drake, *Tearing mode velocity braking due to resonant magnetic perturbations.* Nuclear Fusion, 2012. **52**(103014).

17. J.D. Callen, A. J. Cole, and C.C. Hegna, *Resonant magnetic perturbation effects on pedestal structure and ELMs.* Nuclear Fusion, 2012, **52**(114005).
18. D. P. Schissel, G. Bramson, J. C. DeBoo, *Physics analysis database for the DIIID tokamak.* Rev. Sci. Instrum., 1986. **57**(8).
19. R. A. Moyer et al., *Edge localized mode control with an edge resonant magnetic perturbation.* Physics of Plasmas, 2005. **12**(056119).
20. T. E. Evans et al., *Changes in fluctuations and transport due to toroidal phase variations of non-axisymmetric magnetic perturnations in DIII-D*, Presented at the U. S. Transport Taskforce Workshop, TTF 2012, 10-13 April 2012, Annapolis, MD.
21. W. M. Solomon, K. H. Burrell, P. Gohil, R. J. Groebner, and L.R. Baylor, *Extraction of poloidal velocity from charge exchange recombination spectroscopy measurements.* Review of Scientific Instruments, 2004. **75**(10): p. 3481-3486.
22. T.N. Carlstrom, J.H.Foote, D.G. Nilson, and B.W. Rice, *Design of the divertor Thomson scattering system on DIIII-D.* Review of Scientific Instruments, 1995. **66**(1): p. 493-495.
23. T. H. Osborne, P.B.Snyder, K. H. Burrell, T. E. Evans, M. E. Fernstermacher, A. W Leonard, R. A. Moyer, M. J. Schaffer, and W. P. West, *Edge stability of stationary ELM-suppressed regimes on DIII-D.* Journal of Physics, 2008. **Conference Series 123**(012014).
24. W. M. Stacey, *A coupled plasma-neutrals model for divertor simulations.* Physics of Plasmas, 1998. **5**(4): p. 1015-1026.
25. W. M. Stacey, *A calculation model for density limits in auxiliary heated, gas fueled tokamaks and application to DIII-D model problems.* Physics of Plasmas, 2001. **8**(8): p. 3673-3688.
26. W. M. Stacey, *Modelling the neutral density in the edge of the DIII-D plasma.* Nuclear Fusion, 2000. **40**(5): p. 965-973.
27. W. M. Stacey, *Structure of the edge density pedestal in tokamaks.* Physics of Plasmas, 2004. **11**(9).
28. W. M. Stacey, *Fusion Plasma Physics*, 2005: WILEY-VCH GmbH & Co, KGaA, Weinheim.
29. W. M. Stacey, R.J.Groebner, and T. E. Evans, *Non-diffusive transport in the tokamak edge pedestal.* Nuclear Fusion, 2012. **52**(114020).
30. W. M. Stacey, *The effect of ion orbit loss and X-loss on the interpretation of ion energy and particle transport in the DIII-D edge plasma.* Physics of Plasmas, 2011. **18**(102504).
31. W. M. Stacey, J.A.Boedo, B. A. Grierson, T. E. Evans, and R. J. Groebner, *Intrinsic rotation produced by ion orbit loss and X-loss* Physics of Plasmas, 2012. **19**(112503).
32. J.S. deGrassie, S.H.Miller, and J.A. Boedo, *Plasma flow due to a loss-cone distribution centered around the outboard edge in DIII-D.* Nuclear Fusion, 2011. **52**(013010).
33. W. M. Stacey and R. J. Groebner, *Interpretation of edge pedestal rotation measurements in DIII-D.* Physics of Plasmas, 2008. **15**(012503).